Insights into the role of Nup62 and Nup93 in assembling cytoplasmic ring and central transport channel of the nuclear pore complex

Pankaj K. Madheshiya, Ekta Shukla, Jyotsana Singh, Shrankhla Bawaria, Mohammed Yousuf Ansari[†], and Radha Chauhan[ID]*
National Centre for Cell Science, Pune 411007, Maharashtra, India

ABSTRACT The nuclear pore complex (NPC) is a highly modular assembly of 34 distinct nucleoporins (Nups) to form a versatile transport channel between the nucleus and the cytoplasm. Among them, Nup62 is known as an essential component for nuclear transport, Nup93 for proper nuclear envelope assembly. These Nups constitute various NPC subcomplexes such as the central transport channel (CTC), the cytoplasmic ring (CR), and the inner ring (IR). However, how they play their roles in NPC assembly and transport activity is not clear. Here we delineated the interacting regions and conducted biochemical reconstitution and structural characterization of the mammalian CR complex to reveal its intrinsic dynamic behavior and a distinct "4"-shaped architecture resembling the CTC complex. Our in vitro reconstitution data demonstrate that the Nup62 coiled-coil domain is critical to form both $Nup62^{322\text{-}525}$ •$Nup88^{517\text{-}742}$ and $Nup62^{322\text{-}525}$•$Nup88^{517\text{-}742}$•$Nup214^{693\text{-}926}$ heterotrimers and both can bind to $Nup93^{1\text{-}150}$. We therefore propose that Nup93 acts as a "sensor" to bind to Nup62 shared heterotrimers including the Nup62•Nup54 heterotrimer of the CTC, which was not shown previously to be an interacting partner. Altogether, our biochemical study suggests that Nup62 via its coiled-coil domain is central to form compositionally distinct yet structurally similar heterotrimers and Nup93 binds these diverse heterotrimers nonselectively.

INTRODUCTION

Nuclear pore complexes (NPCs) function as the exclusive gateways between the nucleus and the cytoplasm to facilitate bidirectional nucleocytoplasmic transport (Rout *et al.*, 2000; Beck and Hurt, 2017). The NPCs are highly modular and intricate structures ranging from ~60 MDa in yeast to ~120 MDa in humans (Cronshaw *et al.*, 2002; Alber *et al.*, 2007) and are composed of about 34 distinct nucleoporins (Nups), which are present in multiple copies to form an eightfold rotational symmetric core across the nucleocytoplasmic axis. These Nups are arranged in various subcomplexes to carry out

the distinct biologically conserved functions such as messenger ribonucleoprotein particle (mRNP) export into the cytoplasm and transport of cargoes into and out of the nucleus (Hoelz *et al.*, 2011; Grossman *et al.*, 2012; Beck and Hurt, 2017; Schwartz, 2017; Lin and Hoelz, 2019). Although radially symmetric, the NPC shows nuclear-cytoplasmic asymmetry and is composed of three structural features: a nuclear ring (NR) with a nuclear basket that extends into the nucleoplasm, a central transport channel (CTC) along with inner ring Nups, and a cytoplasmic ring (CR) with filaments that stretch out into

the cytoplasm (Supplemental Figure S1). Detailed knowledge of NPC structure is a prerequisite for mechanistic understanding of its function. The unusually large size of the NPC, together with its conformational plasticity, represents a challenge for determination of its three-dimensional (3D) structure at atomic resolution. Moreover, the complete interaction network of NPC components and their biochemical behavior is still not fully understood. These bottlenecks have significantly hampered the basis for modular NPC assembly and its role in versatile transport functions.

Throughout the vertebrates, a major component of the CR is the Nup88 complex harboring three proteins, Nup62, Nup88, and Nup214 (Supplemental Figure S1). Both Nup88 and Nup214 possess an N-terminal β-propeller domain followed by an α-helical region (Figure 1, A and C). Additionally, Nup214 contains an extensive unstructured FG repeat region at its C-terminal (Figure 1C). On the other hand, Nup62 possesses an N-terminal unstructured region with FG repeats and a C-terminal α-helical region (Figure 1B). These three proteins in the Nup88 complex (Nup88•Nup62•Nup214) are suggested to interact via coiled-coil domains (Huang *et al.*, 2020). Various mRNA export factors that are important for mRNP remodeling bind at the CR of the NPC before translation (Belgareh *et al.*, 1998; Bailer *et al.*, 2000; Hutten and Kehlenbach, 2006; Napetschnig *et al.*, 2007; Kalverda *et al.*, 2010). Moreover, Nup214 and Nup88 are also associated with various human neurological disorders, cardiac diseases, and cancers (Köhler and Hurt, 2010; Yarbrough *et al.*, 2014; Ciomperlik *et al.*, 2015; Nofrini *et al.*, 2016; Lin and Hoelz, 2019). However, the detailed mechanistic function of these Nups with the diseases is not characterized. Interaction studies of the Nup88 complex with other neighboring Nups are limited, except for reports from lower eukaryotes such as *Saccharomyces cerevisiae* and *Chaetomium thermophilum*. The homologue of the Nup88 complex in fungi is known as the Nup82 complex, containing Nup82 (Nup88), Nup159 (Nup214), and Nsp1 (Nup62). Cross-linking mass spectrometry data suggest the presence of an interdomain interaction network between the subunits of the Nup82 complex and with the linker Nups (such as Nup98, Nup145C, and Nup145N) that are responsible for NPC assembly (Gaik *et al.*, 2015; Teimer *et al.*, 2017). Moreover, x-ray crystallographic structures of the fragments of some of these Nups and their complexes, such as Nup82NTD•Nup159Tail with Nup116CTD, Nup145N, and Nup98APD, are available (Napetschnig *et al.*, 2007; Yoshida *et al.*, 2011; Stuwe *et al.*, 2012, 2016a,b). Negative stain electron microscopy (EM) of the fungal Nup82 complex has revealed an overall "P" or "D" shape architecture for this complex (Gaik *et al.*, 2015; Fernandez-Martinez , 2016). However, in the case of metazoans, cryoelectron tomographic (Cryo-ET) reconstructions of the *Xenopus laevis* CR (Huang *et al.*, 2020; Fontana *et al.*, 2022) resolved at ~8 Å showing the positioning of the Nup88•Nup62•Nup214 complex along with the IR complex (Nup93, Nup205, Nup188, Nup155, and Nup35) and the Y-shaped complex (Nup107, Nup133, Sec13, Seh1, Nup160, Nup43, Nup96, Nup75, and Nup37) are available. Similar tomography maps from *Homo sapiens* (Bui *et al.*, 2013; Hurt and Beck, 2015; Von Appen *et al.*, 2015; Kosinski *et al.*, 2016; Schuller *et al.*, 2021) are available lately showing proximity of the CR, IR, and Y shape complexes. However, in these cases, precise interdomain interactions and the biochemical behavior of CR and IR complexes have not been understood yet. Limitations in purifying these stable complexes have impeded the attempts to pursue structural studies for the mammalian complexes.

Recent studies have demonstrated the diverse nature of Nups in different species (Eibauer *et al.*, 2015; Von Appen *et al.*, 2015; Kim *et al.*, 2018; Mosalaganti *et al.*, 2018; Chopra *et al.*, 2019; Field and
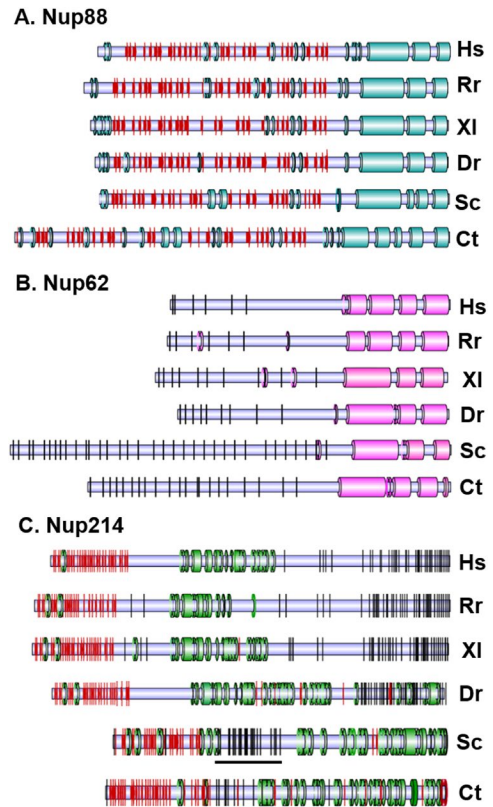

FIGURE 1: Secondary structure organization of the Nup88, Nup62, and Nup214 sequences: organization of secondary structure domains for Nup88 (A), Nup62 (B), and Nup214 (C) from species *Hs, Homo sapiens; Rn, Rattus norvegicus; Xl, Xenopus laevis; Dr, Danio rerio; Sc, Saccharomyces cerevisiae; Ct, Chaetomium thermophilum*. Predicted α-helical domains are represented by cylinders, and β-sheets are represented by red color. FG repeats in the sequences are represented by vertical black lines. The FG repeats sandwiched between the helical region and the β-propeller region in Nup214 sequences of *Saccharomyces* and *Chaetomium* are underlined in black.

Rout, 2019). There are significant differences in the arrangement and architecture of CR Nups in different organisms. Evidence from the vertebrate *X. laevis* shows that the Nup88 complex adopts a "rake-shaped" structure that is different from those of fungi, where the corresponding homologue's two copies (Nup82 complex) are arranged in a parallel manner (Tai *et al.*, 2022). In another study (Bley *et al.*, 2022), it is shown that both yeast and corresponding human heterotrimeric Nup88 complexes have a "P"- or "4-shaped" structure. Further, the mechanisms for the attachment of the CR complexes in *C. thermophilum* NPC are distinct from those of the vertebrates where Nup358 is wrapped around the CR to form the cytoplasmic filaments (Tai *et al.*, 2022).

As the Nup88•Nup62•Nup214 complex is central to the CR, we explored detailed interaction studies followed by biochemical reconstitution of this mammalian complex to understand the role of individual Nups. To characterize the interaction networks, we performed the in silico protein–protein interaction prediction using the CoRNeA (coevolution random forest and network analysis) platform (Chopra *et al.*, 2020) coupled with in vitro tandem affinity pull-down (TAP) assays and dissected the interdomain interactions among these three Nups. Our study revealed that the α-helical coiled-coil regions of these proteins are critical to form the stable complexes

of Nup88[517-742]•Nup62[322-525] and Nup88[517-742]•Nup62[322-525]•Nup214[693-926]. Further, we purified these complexes and performed size exclusion chromatography coupled with multiangle light scattering (SEC-MALS) and circular dichroism (CD) measurements to uncover the varying oligomeric status and thermal stabilities. These reconstituted complexes were subjected to structural analysis using small-angle x-ray scattering (SAXS) and EM, demonstrating the overall architecture of mammalian Nup88[517-742]•Nup62[322-525] and Nup88[517-742]•Nup62[322-525]•Nup214[693-926] heterotrimers. Notably, we observed a significant similarity between the structures of the Nup88[517-742]•Nup62[322-525]•Nup214[693-926] heterotrimer and the earlier reported Nup62•Nup54•Nup58•Nup93[1-819] complex, which led us to establish that the Nup93 can bind to Nup62 shared compositionally different heterotrimers such as Nup88[517-742]•Nup62[322-525], Nup88[517-742]•Nup62[322-525]•Nup214[693-976], Nup62•Nup54•Nup58, and Nup62[322-525]•Nup54[181-507]. Thus, our data here illustrate the hub role of Nup62 to form distinct heterotrimers and of Nup93, which behaves as a sensor in recognizing these Nup62 shared heterotrimers, thereby assembling the CR and CTC complexes of the mammalian NPC.

RESULTS

Divergence in the sequences of Nup88 complex across phyla

The phylogenetic analysis of Nup88, Nup62, and Nup214 protein sequences from a total of 38 different organisms showed that Nups from humans, rats, and other vertebrates such as *Xenopus and Danio* species clustered distantly from the branches of *Chaetomium* and *Saccharomyces* (Supplemental Figure S2, a, b, and c and Table S1). The metazoan clade marks close proximity and similarity among various organisms from different phyla. Accordingly, the secondary structure prediction of Nup88, Nup62, and Nup214 from different organisms ranging from fungi to humans displays the differences and similarities in domain organization of these Nups in different organisms (Figure 1, A and C). It is observed that the α-helical region in the mammalian Nup214 is shortened when compared with unicellular eukaryotes (Supplemental Figure S3). In mammals, this helical region is sandwiched between the propeller domain and the FG region, whereas in fungi, it is present at the C-terminal end (Figure 1C). As reported previously (Chopra *et al.*, 2019), we noticed that there are significant divergences in the primary sequence identity between the Nups of fungi and vertebrates (Supplemental Table S2). Thus, we concluded that although some of the domains and folds remain conserved, there are distinct species-specific features evident among these Nups' homologues from unicellular eukaryotes to vertebrates.

Establishing the interacting interface among Nup88, Nup214, and Nup62

Earlier, we developed a computational tool, CoRNeA, which can predict binary interacting interfaces solely based on primary protein sequences (Chopra *et al.*, 2020). We employed this tool to predict precise interacting regions among Nup88, Nup214, and Nup62. A concatenated multiple sequence alignment file (only structured regions) of two interacting partners, namely: Nup62•Nup88, Nup88•Nup214, and Nup214•Nup62, was used in the CoRNeA workflow as described previously (Chopra *et al.*, 2020). The final interface outputs were sorted based on the convolution scores as high scoring residue pairs indicating a very high probability of these residue pairs to form the interactive interface between the two proteins (Supplemental Figure S4). A summarized representation of such interdomain interactions is depicted in Figure 2A. Overall we
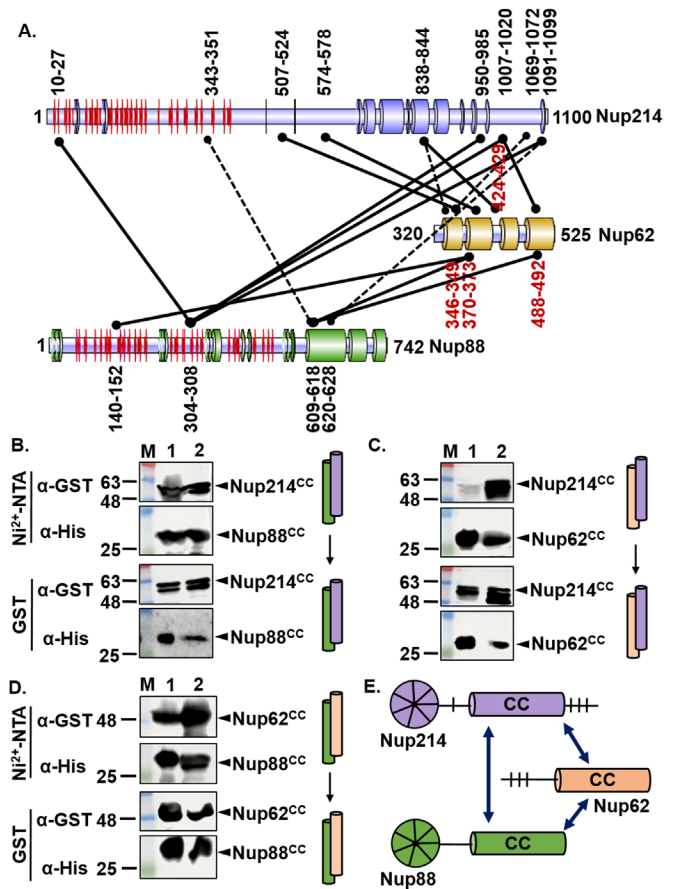

FIGURE 2: Interaction mapping among Nup88, Nup62, and Nup214 coiled-coil regions. (A) Schematic depiction of various interdomain interactions between Nup88[517-742] (purple), Nup214[693-976] (green), and Nup62[322-525] (orange) by the in silico tool CoRNeA. The helices are represented by cylinders, and β-sheets are represented by red color. Interacting residue pairs are marked on the respective domains. High convolution score predictions are marked by solid lines, while low score predictions are represented by dashed lines. (B–D) Western blot scan showing tandem affinity pull down (Ni^{2+}-NTA followed by GST affinity) of coiled-coil domains (depicted as cylinders) of Nup88[517-742], Nup62[322-525], and Nup214[693-976]. Schematic representation of Nup88 (green) and Nup62 (orange) coiled-coil interactions as cylinders are shown. (BGST-tagged Nup214[693-976] interaction with His6- tagged Nup88[517-742]. (C) GST-tagged Nup214[693-976] interaction with His6-tagged Nup62[322-525]. (D) His6-tagged Nup88[517-742] association with GST-tagged Nup62[322-525]. (E) Cartoon summarizing interaction results of CoRNeA prediction and pull-down experiments. Lanes M, 1, and 2 represent marker, input, and eluent, respectively. Coiled-coil domain represented by "CC" and β-propeller domain by "β" symbol.

observed that the Nup62 coiled-coil region forms an extensive interaction network with the coiled-coil region of Nup88 and Nup214. Similarly, the β-propeller domains of Nup88 and Nup214 are capable of interacting with each other; however, fewer contacts were formed between Nup62 coiled-coil regions with the β-propellers of Nup214 and Nup88. The detailed pairwise interaction analysis is described as follows.

Nup88 and Nup214 interface. For this pair, based on the convolution scores (Supplemental Figure S4a), the strongest interacting regions were predicted for Nup88[β-propeller] (304–308 amino acid residues) with Nup214[β-propeller] (10–27) and Nup214[coiled-coil] (950–1099

amino acid residues). Low scores were obtained for regions Nup-88[coiled-coil] (611–628) interacting with Nup214[coiled-coil] (1091–1100) and Nup214[β-propeller] (201–351) (Supplemental Figure S4a). Overall, this indicated that both the β-propeller and the coiled-coil domain of Nup214 and Nup88 can interact with each other.

Nup214 and Nup62 interface. CoRNeA of this pair revealed that the α-helical region of Nup62 (370–490) has strong interaction with Nup214[coiled-coil] (685–1072). Very low convolution scores were obtained for Nup214[β-propeller] with Nup62[coiled-coil], indicating low possibility of direct interactions among them (Supplemental Figure S4b).

Nup88 and Nup62 interface. A very strong interaction between Nup62 and Nup88 was observed. A high convolution score suggests that Nup62[coiled-coil] (370–492) and Nup88[coiled-coil] (609–626) have strong interaction between them. Interestingly, CoRNeA also predicted an interface for Nup62[coiled-coil] (370–373) and Nup88[β-propeller] (140–152) with high scores (Supplemental Figure S4c).

Pull-down approach delineates the interdomain interaction network among Nup88, Nup62, and Nup214

To test the CoRNeA-predicted domain interactions, we evaluated their in vitro binding capability using the TAP assay. In each case, we cotransformed the recombinant plasmids harboring specific regions of two Nups fused with two different tags (GST and His$_6$). Then we performed protein overexpression and subsequently tandem affinity purification (Ni^{2+}-NTA pull down in series with GST pull down) to analyze their interaction with each other. Further, the interactions were confirmed either by Coomassie staining of SDS–PAGE or by Western blotting using anti-His and anti-GST antibodies. We have used a total of six constructs for the interaction analysis using the TAP method, the coiled-coil domains His$_6$- and GST-tagged Nup62[522-325], His$_6$- tagged Nup88[517-742], and GST-tagged Nup214[693-976]; the β-propeller domains His$_6$-tagged Nup88[59-498] and GST-tagged Nup214[1-407]. Out of these, Nup214[693-976] alone could not be expressed in soluble form (unpublished data). So we proceeded with the remaining constructs to rule out their nonspecific interactions with the affinity resins (Supplemental Figure S5) and found that none of these constructs is interacting with the affinity resins nonspecifically. Also to be noted is that all the pull-down experiments were performed under identical conditions including buffers, bacterial culture conditions, and equipment.

The coiled-coil domains of the Nup88, Nup62, and Nup214 interact in a stable manner. Plasmids containing GST-tagged Nup214[693-976] were cotransformed with either His$_6$-tagged Nup62[322-525] or Nup88[517-742] for tandem affinity purification followed by Western blotting as well as Coomassie-stained SDS–PAGE analysis. We observed that the coiled-coil region of Nup214[693-976] has a stable interaction with the coiled-coil regions of Nup88[517-742] and Nup62[322-525] (Figure 2, B and C; Supplemental Figure S6, a and b). In another parallel set of pull-down experiments, the GST-tagged Nup62[322-525] region was coexpressed with the His$_6$- tagged Nup88[517-742]. They were also subjected to similar analysis, and physical interaction was seen between the coiled-coil regions of these two Nups (Figure 2D). Thus, it became evident (Figure 2E) that the coiled-coil domains of Nup88[517-742], Nup214[693-976], and Nup62[322-525] are capable of forming stable complexes, as they are not washed away during the two steps of the purification (Supplemental Figure S6 and Figure 2). Furthermore, this analysis validated our in silico predictions (Figure 2A), where we noticed a high convolution score for the coiled-coil domains of Nup62 and Nup88 (Supplemental
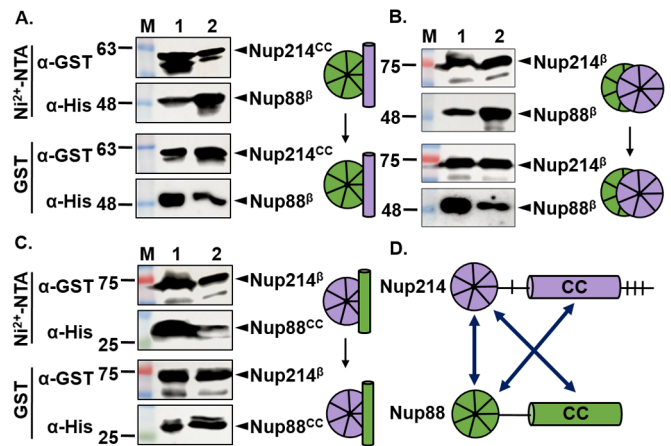

FIGURE 3: Interaction mapping of coiled-coil and β-propeller domains of Nup88 with Nup214. (A–C) Western blot scan showing tandem affinity pull down (Ni^{2+}-NTA followed by GST affinity) of Nup88 (green) and Nup214 (purple). Schematic representation of coiled-coil domain of Nup88[517-742] (green) and Nup214[693-976] depicted by cylinders and β-propeller domains of Nup88[59-498] (green) and Nup214[1-407] depicted by circles. (A) GST-tagged Nup214[693-976] interaction with His$_6$-tagged Nup88[59-498]. (B) GST-tagged Nup214[1-407] interaction with His$_6$-tagged Nup88[59-498]. (C) GST-tagged Nup214[1-407] interaction with His$_6$-tagged Nup88[517-742]. (D) Cartoonsummarizing interaction results of the CoRNeA prediction and pull-down experiments. Lanes M, 1, and 2 represent marker, input, and eluent, respectively. Coiled-coil domain represented by "CC" and β-propeller domain by the "β" symbol.

Figure S4c) and relatively lower convolution scores for the coiled-coil domains of the Nup214 and Nup62 interface (Supplemental Figure S4b).

β-Propeller and α-helical domains of Nup88 and Nup214 interact with each other. The β-propeller domain of Nup88[59-498] was coexpressed as a His$_6$-tagged fusion protein with either the β-propeller or helical domain of Nup214 viz. Nup214[1-407] and Nup214[693-976], which were fused with the GST tag. They were processed by the TAP method as described above. We found that the β-propeller region of Nup88[59-498] was able to pull down both the β-propeller and the coiled-coil regions of Nup214, forming probable α/β and α/α associations, respectively (Supplemental Figure S7). To rule out nonspecific interactions of the proteins, we also performed a pull-down assay using the combination of His$_6$-tagged Nup88 with the pGEX4T1 plasmid (expressing the GST protein alone) and observed that the β-propeller domain of Nup88[59-498] does not interact with the GST protein (Supplemental Figure S5e). These interactions between the β-propeller domain of Nup88[59-498] and Nup214[1-407] appear to be biochemically stable in both the Coomassie-stained SDS–PAGE and corresponding Western blotting analyses of the coeluting fractions (Figure 3, A and B; Supplemental Figure S7c). Similarly, in the case of Nup214[1-407] coexpressing with Nup88[517-742], we noticed that both proteins were interacting stably (Figure 3C). Taking together these data and in silico interface prediction data (Figure 2A), we concluded that the β-propeller and coiled-coil domains of both Nup88 and Nup214 interact with each other, making a lengthwise strong connection (Figure 3D).

Coiled-coil domain of Nup62 interacts transiently with β-propeller domains of Nup214 and Nup88. The β-propeller region of Nup88 is identified as 59–498 amino acids long, and the
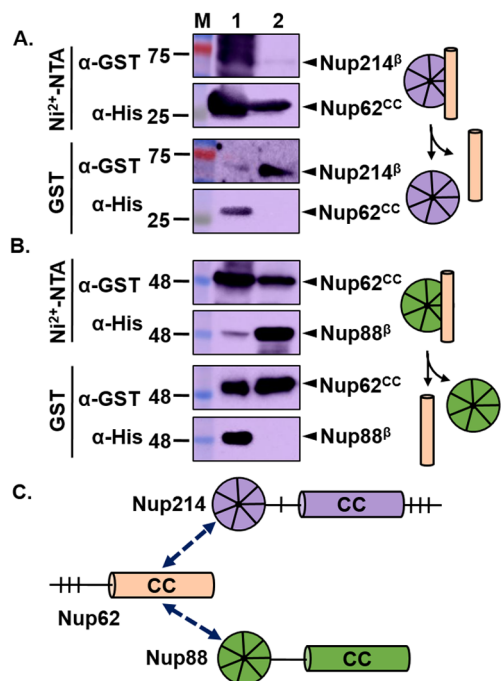
FIGURE 4: Mapping interaction of Nup62 coiled-coil domain with β-propeller domains of Nup88 and Nup214. (A, B) Western blot scan showing tandem affinity pull down (Ni^{2+}-NTA followed by GST affinity) of Nup88 (green), Nup62 (orange), and Nup214 (purple). Schematic representation of Nup88$^{59-498}$ and Nup214$^{1-407}$ β-propeller domain depicted as circles, helical regions of Nup62$^{322-525}$ as cylinders. (A) GST-tagged Nup214$^{1-407}$ showed transient interaction with His$_6$-tagged Nup62$^{322-525}$. (B) GST-tagged Nup62$^{322-525}$ has a weak interaction with His$_6$-tagged Nup88$^{59-498}$. In both cases, one of the partners is washed away during the second round of purification. (C) Cartoon summarizing interaction results of CoRNeA prediction and pull-down experiments. Lanes M, 1, and 2 represent marker, input, and eluent, respectively. Coiled-coil domain represented by "CC" and β-propeller domain by the "β" symbol.

β-propeller region of Nup214 is 1–407 amino acids. When the coelution of the Nup62$^{322-525}$ with the β-propeller regions of Nup214$^{1-407}$ and Nup88$^{59-498}$ was analyzed, we observed that the bands of His$_6$-tagged Nup62$^{322-525}$ and Nup88$^{59-498}$ were washed off in a second (GST) affinity step (Figure 4, A and B), suggesting a relatively transient interaction between these domains (Figure 4C). Similar weak or no interaction was also observed in our CoRNeA-based prediction analysis (Figure 2A). Thus, we conclude that the Nup62$^{322-525}$ domain is not able to form a stable complex with either Nup214$^{1-407}$ or Nup88$^{59-498}$.

α-Helical domains are sufficient for Nup88•Nup62•Nup214 complex reconstitution

On the basis of our in silico and pull-down analyses, we established that the coiled-coil regions of Nup88, Nup62, and Nup214 are capable of interacting with each other. Additionally, to accomplish biochemical reconstitution of Nup88$^{517-742}$•Nup62$^{322-525}$•Nup214$^{693-976}$ complex assembly, we coexpressed and purified the helical regions of these Nups (Figure 5A). The tandem affinity–purified proteins (Figure 5, B and C) were subjected to size exclusion chromatography (SEC) after affinity tag removal, which indicated the formation of a stable yet dynamic complex under the given biochemical conditions (Figure 5D). We found ambiguity in validating the presence of all three Nups on the Coomassie-stained SDS–PAGE as it showed
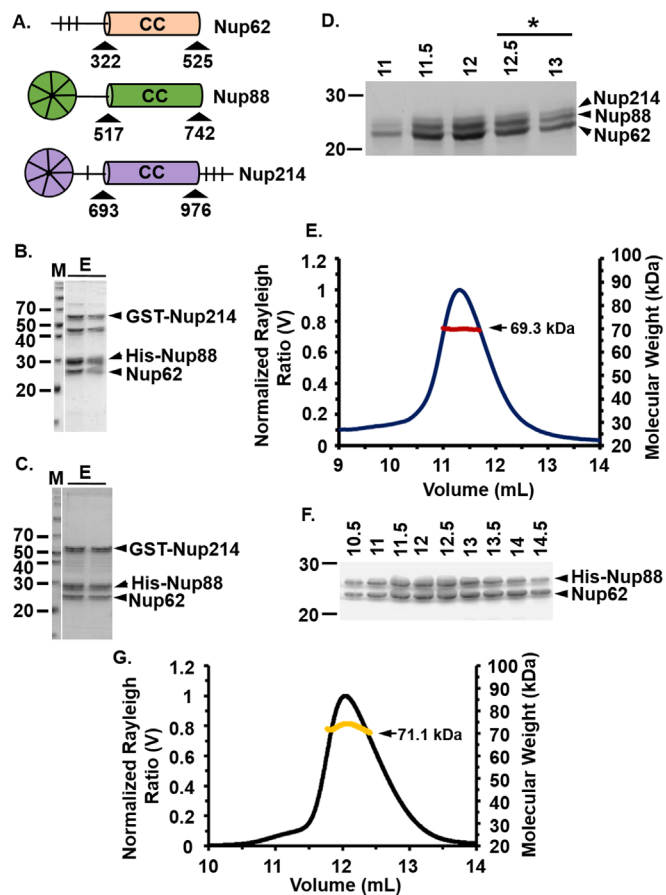

FIGURE 5: Purification of the Nup88•Nup62 and Nup88•Nup62 •Nup214 complexes: (A) Diagrammatic depiction of domain boundaries of Nup62$^{322-525}$, Nup88$^{517-742}$ and Nup214$^{693-976}$ used for cloning, co-expression and purification. (B) SDS–PAGE showing the purified heterotrimeric Nup88$^{517-742}$•Nup62$^{322-525}$•Nup214$^{693-976}$ complex via Ni^{2+}-NTA affinity purification followed by (C) GST affinity purification. (D) 12% SDS–PAGE scan showing the SEC peak eluted fractions (ml) of the Nup88$^{517-742}$•Nup62$^{322-525}$•Nup214$^{693-926}$ complex. (E) SEC-MALS analysis of the Nup88$^{517-742}$•Nup62$^{322-525}$•Nup214$^{693-926}$ complex showing the Rayleigh scattering in black and molecular weight distribution across the peak in red color. (F) 12% SDS–PAGE scan showing the SEC eluted peak fractions (ml) of the Nup88$^{517-742}$ •Nup62$^{322-525}$ complex. (G) SEC-MALS analysis of the Nup88$^{517-742}$ •Nup62$^{322-525}$ complex showing Rayleigh scattering in black while yellow color marks molecular weight distribution across the peak; the SEC eluted fractions used for the negative stain EM analysis represents by asterisk underline and coiled-coil domain by "CC."

the presence of the Nup62$^{322-525}$ corresponding band as well as two closely placed bands for Nup88$^{517-742}$ and Nup214$^{693-976}$ (below the 30 kDa weight marker; Figure 5D). It seemed that all three proteins (with theoretical molecular weight: Nup88$^{517-742}$ = 26.6 kDa; Nup62$^{322-525}$ = 23.7 kDa; and Nup214$^{693-976}$ = 32.8 kDa) migrated very close to each other. Therefore, these proteins were further subjected to Orbitrap mass spectrometry, where trypsin-digested fragments of all three Nups were detected as the top hits (Supplemental Figure S8, a and b, and Supplemental Table S3). This mass spectroscopy–based analysis revealed that the purified Nup214$^{693-976}$ is truncated at the C-terminus (due to nonspecific thrombin cleavage) and its boundary shifted to 693–926 instead of 693–976. This led to alter the observed molecular weight of Nup214$^{693-926}$ to 27.4 kDa, thus migrating very closely to the observed Nup88$^{517-742}$ band (26.6 kDa). Overall, the formation of a trimeric complex

(Nup88$^{517-742}$•Nup62$^{322-525}$•Nup214$^{693-926}$) by in vitro reconstitution was confirmed. Additionally, we observed variation in the ratio of Nup62$^{322-525}$, Nup88$^{517-742}$, and Nup214$^{693-926}$ on the SEC-eluted peak profile (Figure 5D); the peak fraction eluted at 11.0 ml showed only two bands corresponding to Nup62$^{322-525}$ and Nup88$^{517-742}$, and 12–13 ml peak fractions showed bands corresponding to Nup88$^{517-742}$, Nup62$^{322-525}$, and Nup214$^{693-926}$. This clearly indicated that the purified trimeric complex is a mixture of several stoichiometric combinations of heterotrimers, such as Nup88$^{517-742}$•Nup62$^{322-525}$ and Nup88$^{517-742}$•Nup62$^{322-525}$•Nup214$^{693-926}$. To further understand the dynamics, the purified complexes and individual components were subjected to SEC-MALS analysis and glutaraldehyde cross-linking as described below.

Establishing the oligomeric status of the Nup88•Nup62•Nup214 complex

We have earlier reported that the coiled-coil region of Nup62$^{322-415}$ exists in a dynamic equilibrium between trimer and dimer (Dewangan *et al.*, 2017). Further, the sequences of Nup88 and Nup214 when analyzed by MULTICOIL2 indicated that the propensity of these nucleoporins to form trimers is greater than that for dimers. To understand the oligomeric properties of individual proteins, we purified them separately as Nup62$^{322-525}$ and Nup88$^{517-742}$ (Supplemental Figure S9, a and b). The purification of Nup214$^{693-976}$ alone did not yield a soluble form of the protein (unpublished data). We therefore concluded that Nup214$^{693-976}$ certainly needed an interacting partner to remain in a soluble form. Consistent with this MULTICOIL2 prediction, SEC-MALS analysis of His$_6$-tagged Nup88$^{517-742}$ (theoretical molar mass 26.6 kDa) indicated two peaks ranging from 75 to 50 kDa, suggesting a dynamic equilibrium between trimeric and dimeric forms, respectively (Supplemental Figure S9c). Also, the peak for the trimer was much higher when compared with that of the dimer. Similarly, the purified Nup88$^{517-742}$•Nup62$^{322-525}$•Nup214$^{693-926}$ complex, when analyzed using SEC-MALS, showed the average molar mass of 69.3 kDa (theoretical mass 77.6 kDa = Nup62:23.7+Nup88:26.6+Nup214:27.4) (Figure 5E), which suggests that the complex is likely to be a heterotrimer with several possibilities of combinations: one copy each of Nup88$^{517-742}$, Nup62$^{322-525}$, and Nup214$^{693-926}$ or two copies of Nup62$^{322-525}$ or Nup88$^{517-742}$ with a single chain of Nup88$^{517-742}$, Nup62$^{322-525}$, respectively. We used two different concentrations of the complex (0.4 and 1.4 mg/ml) to rule out the concentration-dependent variations and found the averaged molar mass to be consistent (Supplemental Table S4). We further attempted to understand the stoichiometry using the glutaraldehyde cross-linking analysis, which revealed a protein band (in smear manner) corresponding to 75 kDa (Supplemental Figure S10). Thus we concluded that various combinations of heterotrimers such as Nup62$^{322-525}$•Nup88$^{517-742}$•Nup214$^{693-926}$ (theoretical 77.5 kDa in 1:1:1 stoichiometry), Nup88$^{517-742}$•Nup62$^{322-525}$ (theoretical 73.8 kDa with 2:1 stoichiometry), and Nup62$^{322-525}$•Nup214$^{693-926}$ (theoretical 74.6 kDa with 2:1 stoichiometry) appear to have very close molecular weights to be separated in our cross-linking experiments and hence appeared as a smear band ranging from 70 to 80 kDa. Overall, we observed that none of these methods was capable of differentiating various heterotrimers existing in the purified Nup62$^{322-525}$•Nup88$^{517-742}$•Nup214$^{693-926}$ complex. However, a significant population of the Nup62$^{322-525}$•Nup88$^{517-742}$•Nup214$^{693-926}$ complex (1:1:1 stoichiometry) would coexist with other heterotrimeric combinations (Figure 5, D and E, and Supplemental Figure S10). In the case of *X. laevis*, the Nup88•Nup62•Nup214 heterotrimer model was fitted into the EM density map, which indicated the coiled-coils from three core proteins of the Nup88 complex (Huang *et al.*, 2020).

Data collection parameters	
Beamline	BM29
Detector	Pilatus 1 M
Wavelength (λ), Å	0.991
Detector-to-sample distance, m	2.867
Q-range, nm^{-1}	0.035–4.94
No. of frames collected	10
Exposure time per frame, s	0.5
Measurement temperature, K	277
Concentration range, mg/ml	0.9
Concentration range, µM	11.5
Structural parameters	
Guinier analysis	
R_g, nm	7.1
R_c, nm	2.15
L, nm	23.44
Indirect Fourier transformation P(r)D_{max}, nm	36.39
R_g, nm	8.45
Porod exponent estimate	2
Modeling parameters	
χ^2 value of DAMFILT model with raw data (CRYSOL)	2.88
DAMMIF (10 models) NSD	1.031 ± 0.132

TABLE 1: SAXS data collection, structure solution, and model parameters for the Nup88•Nup62 complex.

Furthermore, fungal species–based studies also revealed stoichiometry of corresponding homologous complexes in fungi in 1:1:1 stoichiometry (Fischer *et al.*, 2015; Gaik *et al.*, 2015). This indicates that the propensity of these Nups to form a heterotrimer is evolutionarily conserved; however, a significant intrinsic plasticity in the Nup88 complex is evident in our study to form a distinct combination of the heterotrimers.

Coiled-coil domains of Nup88 and Nup62 also form a dynamic heterotrimer

On the basis of our protein–protein interaction analysis, we observed that the coiled-coil domains of Nup88 and Nup62 interact with each other strongly. The affinity-purified Nup88$^{517-742}$•Nup62$^{322-525}$ complex, when analyzed using SEC methods, showed a homogeneously reconstituted complex (Figure 5F). Further, we obtained a uniform distribution of averaged mass (71.1 kDa) with SEC-MALS (Figure 5G). Because the theoretical mass of the heterodimeric (1:1) complex is 52.8 kDa, we suspect that the complex exists in 1:2 stoichiometry with an additional chain of either Nup62$^{322-525}$ or Nup88$^{517-742}$. To confirm this, we did a densitometric analysis of the SDS–PAGE bands, which clearly specifies that the band intensity corresponding to Nup62$^{322-525}$ is almost twice that of Nup88$^{517-742}$; I, indicating two copies of Nup62$^{322-525}$ in complex with a single Nup88$^{517-742}$ (Supplemental Figure S11).

Solution structure reveals an elongated shape of heterotrimer Nup88•Nup62 complex

To gain further insight into the Nup88$^{517-742}$•Nup62$^{322-525}$ complex structure and dynamicity, we employed the SAXS technique, an
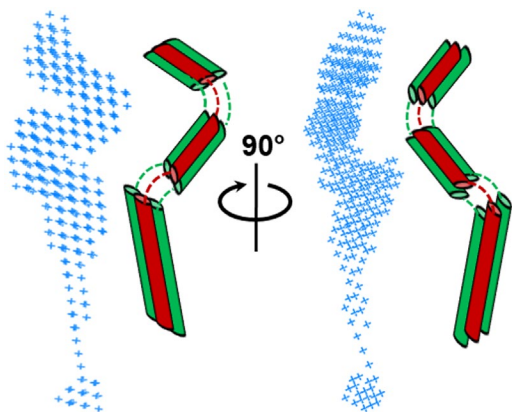
FIGURE 6: SAXS analysis of the Nup88•Nup62 complex. The molecular envelope of the Nup88$^{517-742}$•Nup62$^{322-525}$ complex was obtained by DAMMIF analysis (shown in blue color). The cartoon model of the protein complex (two copies of the Nup62 in green color and one copy of the Nup88 in red) is shown in two different orientations.
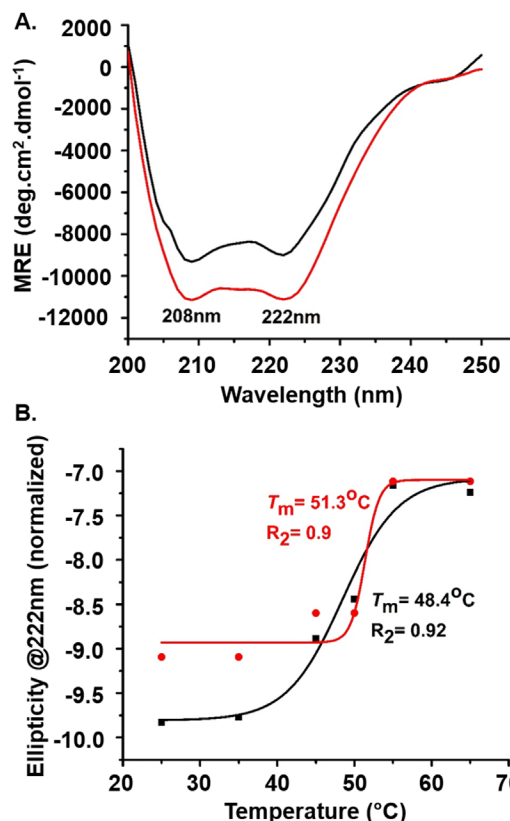

FIGURE 7: CD spectroscopy analysis of the Nup88•Nup62 and Nup88•Nup62•Nup214 complexes. (A) Far-UV CD spectra of purified Nup88$^{517-742}$•Nup62$^{322-525}$ and Nup88$^{517-742}$•Nup62$^{322-525}$•Nup214$^{693-926}$ are shown in black and red color, respectively. (B) Thermal denaturation profile showing T_m for the complexes via a sigmoidal fit of the ellipticity shift at 222 nm. The red color denotes the curve for the Nup88$^{517-742}$•Nup62$^{322-525}$•Nup214$^{693-926}$ complex, while the curve for Nup88$^{517-742}$•Nup62$^{322-525}$ is shown in black.

established method for the structural analysis of dynamic behavior of proteins in solution. We calculated the radius of gyration (R_g) using the low-Q region as well as the radius of cross-section (R_c) by assuming the globular and rod-like shape of the predominant scattering molecules in the solution. By employing $L = [12(R_g^2 - R_c^2)]^{1/2}$ (Table 1), the length of persistence (L) of respective scattering entities was calculated. Further, the double log plot, that is, Log10 I (Q) versus Log10 Q (nm^{-1}), confirmed no interparticle interaction or aggregation (Supplemental Figure S12a). The Guinier analysis, Ln I (Q) versus Q^2, plot is linear, indicating good monodisperse quality of the heterodimeric complex (Supplemental Figure S12b). The slope of the Guinier plot was used to calculate the R_g value of the complex as 7.11 nm (Table 1). The D_{max} was calculated from the pairwise distance distribution plot $P(R)$ using indirect Fourier transformation, and the maximum distance observed is 36.39 nm. The elongated and highly dynamic shape of the $P(R)$ functions confirms the extended state of the complex in solution. The Kratky plot, that is, I(Q)*Q^2 versus Q (nm^{-1}), shows the highly flexible structure of the complex corroborated by Porod exponent (quantitative metric for assessing compactness) value of 2.2 (Supplemental Figure S12, c and d), suggesting a less compact and highly dynamic structure.

On the basis of the SAXS data, we performed dummy atomic modeling (DAMMIF) to build a 3D model of the complex. The final generated model of the complex was compared with the raw data I (Q) profile by using the CRYSOL program. The Chi-square value of 2.88 suggests that the DAMFILT model fits well with the raw data. There are some extra regions observed at the extremities of the SAXS model that could be due to intrinsic flexibility of the protein complex in solution (Figure 6). The high degree of flexibility between the coiled-coil domains of fungal homologue Nup82 with a kinked structure was also reported earlier (Fernandez-Martinez et al., 2016). Additionally, we earlier showed that the coiled-coil domain of Nup62 forms a triple helix bundle (Dewangan et al., 2017), and our SEC-MALS data in this study further suggests that the Nup88$^{517-742}$•Nup62$^{322-525}$ complex exists in 1:2 stoichiometry. Hence, we represented Nup88$^{517-742}$•Nup62$^{322-525}$ as a heterotrimer in 1:2 stoichiometry as shown in Figure 6. It appears that the complex is highly elongated. Overall, our SAXS data clearly indicate that the Nup88$^{517-742}$•Nup62$^{322-525}$ complex possesses a flexible and dynamic behavior in solution and adopts an elongated structure.

Nup88•Nup62 and Nup88•Nup62•Nup214 heterotrimers show variable conformational thermostability

The α-helical coiled-coil is one of the principal subunit oligomerization motifs in proteins. Despite its simplicity, it is a highly versatile folding motif due to which coiled-coil–containing proteins exhibit a broad range of functions (Greenfield and Hitchcock, 1993; Burkhard et al., 2001). We probed the secondary structure and conformational stability of proteins by CD spectroscopy. Wavelength scans showed the α-helical coiled-coil signature with minima at 208 and 222 nm for Nup62$^{322-525}$ and Nup88$^{517-742}$ (Supplemental Figure S9d), the Nup88$^{517-742}$•Nup62$^{322-525}$ complex, and the Nup62$^{322-525}$•Nup88$^{517-742}$•Nup214$^{693-926}$ complex (Figure 7A). The $\theta_{222}/\theta_{208}$ ratio depicts the helix propensity of the proteins. Also, the combination of helix propensity and hydrophobic core packing determines the stability of coiled-coil structures (López-García et al., 2019). So, we calculated the $\theta_{222}/\theta_{208}$ ratios and percent helicity in each case as displayed in Supplemental Table S5a. When the $\theta_{222}/\theta_{208}$ ratio exceeds 1, it indicates a well-defined coiled-coil structure. It is clear from Supplemental Table S5a that the complexes behave very well as a coiled-coil structure in the solution.

To compare the thermostability of the heterodimeric and heterotrimeric complexes, we investigated their thermal denaturation with CD spectroscopy. Examination of the CD signal at 222 nm over a range of temperatures (25–95°C) showed that the Nup88$^{517-742}$•Nup62$^{322-525}$ complex exhibits a T_m of 48°C and the Nup62$^{322-525}$•Nup88$^{517-742}$•Nup214$^{693-926}$ complexes have a T_m of

51°C (Figure 7B), a feature that is consistent with the thermostability of other naturally occurring coiled-coil domains ($T_m \geq 50°C$) (Tsuruda et al., 2011; Fujiwara et al., 2012). It is apparent from the CD denaturation curves that though the unfolding begins, the Nup62[322-525]•Nup88[517-742]•Nup214[693-926] complex retains its helical structure even at higher temperatures (40–45°C). On the other hand, the Nup88[517-742]•Nup62[322-525] complex loses its helical conformation faster and is adopting random coil structure as the temperature increases (Supplemental Table S5b). These results suggest that Nup214[693-926] plays an important role in providing stability to the complex. Moreover, the thermal denaturation was irreversible in all cases (unpublished data).

Structure of the Nup88•Nup62•Nup214 complex revealed by negative stain EM

As we could not pursue SAXS studies of the Nup88[517-742]•Nup62[322-525]•Nup214[693-926] complex due to low solubility, we analyzed the structure of this heterotrimer using negative stain EM. The SEC-purified complex (Figure 5D; 12.5–13 ml peak fraction) was adsorbed on EM grids and stained with 2% uranyl acetate. We anticipated conformational heterogeneity of the complex on the grid, due to the intrinsic plasticity of the Nup88[517-742]•Nup62[322-525]•Nup214[693-926] complex (Figure 8A). Approximately 4737 particles were manually selected and utilized for the single-particle analysis using CryoSPARC. The 2D class averages obtained showed the distinct shape-elongated structures with a curve at one end (Figure 8B). Further, these 2D classes were used for the ab initio 3D reconstruction into two classes, where we found that about 67% of particles were assigned to a distinct shape and compact structure (Figure 8C) and the rest (~33%) of the particles showed a much smaller flattened shape, perhaps due to the preferred orientation issues or highly variability in the shape. Based on the FSC cutoff at 0.143, the global resolution of the structure is 19.27Å (Supplemental Figure S13b). In comparison with SAXS data of the Nup88[517-742]•Nup62[322-525] complex (Figure 6), we observed that the EM 3D map is much more compact in shape (Figure 8C). The final EM map showed an elongated "4" shape with a bulky head. This shape shows similarity with the tube-like density reported for the coiled-coil helix bundle of. the Nup88 complex in Xenopus (Huang et al., 2020) where the authors modeled full-length Nup88 and the coiled-coil domains of Nup62 and Nup214 and fitted them into the tomogram. We obtained the homology models of Nup88, Nup62, and Nup214 from the Alpha-Fold database (Varadi et al., 2022) and built a complex model using the CtNsp1 complex (PDB ID; 5CWS; Stuwe et al., 2016b) as the template. This modeled complex was then docked into the EM density map (Figure 8D), which shows that the model fitted very well in the density map and adopts a "4" shape structure inside the density, which is almost identical to the reported CtNsp1•Nup49•Nup54•Nic96 complex (Stuwe et al., 2016a), where ~41 residues (139–180) of Nic96 (a homologue of Nup93) is located in the bulky head. We also attempted to dock the Nup62[322-525]•Nup88[517-742] heterotrimer into the obtained density but could not find a better fit (unpublished data). Moreover, our previous study (Sonawane et al., 2020) has shown that mammalian Nup93 is capable of forming a quaternary complex with CTC (Nup62•Nup54•Nup58) and a "4"-shaped structure where the CTC complex is aligned parallel to Nup93[1-819]. Interestingly, a feature of "bulky head" was also observed in this case.

Nup88•Nup62 and Nup88•Nup62•Nup214 heterotrimers interact with the N-terminal region of Nup93

The superimposition of the EM density of the CTC•Nup93[1-819] complex (Figure 8E) with the density map obtained for the Nup88
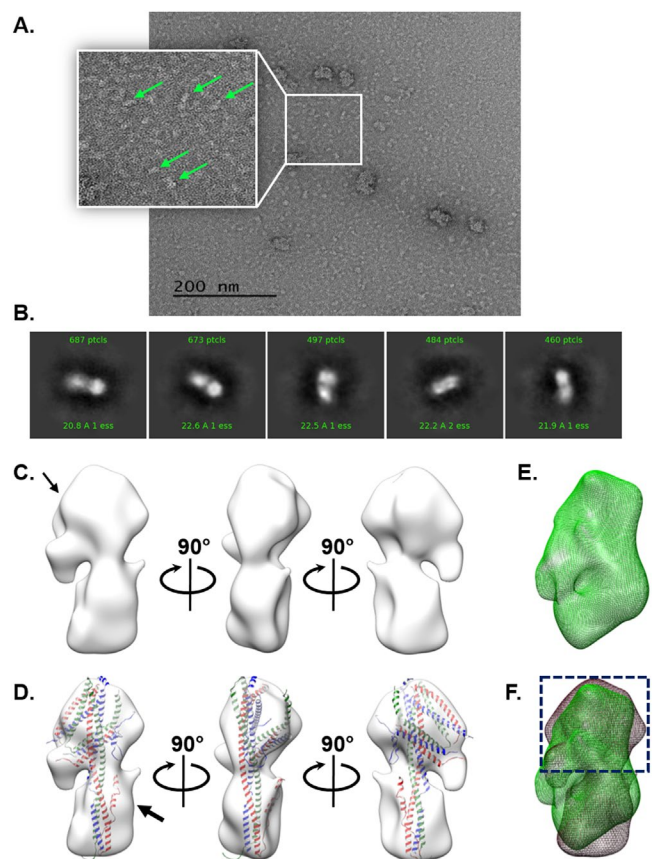

FIGURE 8: Negative staining EM analysis of the Nup88 complex and superposition over the CTC•Nup93 (1–819) complex. (A) Representative micrograph of purified Nup88[517-742]•Nup62[322-525]•Nup214[693-926] complex stained with 2% uranyl acetate. Scale bar: 200 nm. Representative particles used for the analysis are shown in the inset with the arrow. (B) Representative 2D class averages. (C) 3D density map obtained at 19.27 Å. (D) Density map fitted with modeled structures of the coiled-coil complex. The bulky head of the map and N-terminal helix density of Nup214 are shown by the black thin and thick arrow, respectively. In the EM density map Nup214, Nup88, and Nup62 are represented by red, blue, and green color, respectively. (E) 3D density map of the CTC•Nup93[1-819] complex (shown in green color). (F) Superimposed 3D density map of Nup88 complex (gray) over the CTC•Nup93 complex (green). Dash blue box shows the overlapping head region of both complexes.

complex (Figure 8F) revealed that the head regions of both densities match perfectly, indicating similar arrangements of the triple helix bundle formed by both Nup88[517-742]•Nup62[322-525]•Nup214[693-926] and Nup62[322-525]•Nup58[239-415]•Nup54[332-510]. Also it was shown previously (Sonawane et al., 2020) that the 1–150 region of Nup93 is sufficient to form the stable quaternary complex Nup62[322-525]•Nup58[239-415]•Nup54[332-510]•Nup93[1-150]. Hence, on the basis of these observations, we hypothesized that similar to the CTC complex, the Nup88 complex may also bind to the Nup93[1-150], and we evaluated whether Nup93[1-150] can interact with either or both Nup88[517-742]•Nup62[322-525] and Nup88[517-742]•Nup62[322-525]•Nup214[693-926] heterotrimers. We performed TAP of both these complexes with the Nup93[1-150] domain. Surprisingly, we observed the N-terminus of Nup93[1-150] forming a stable complex with both the Nup88[517-742]•Nup62[322-525] heterotrimer (Figure 9, A and B) as well as the Nup88[517-742]•Nup62[322-525]•Nup214[693-976] heterotrimer (Figure 9, C and D). Our finding seems to be in agreement with a
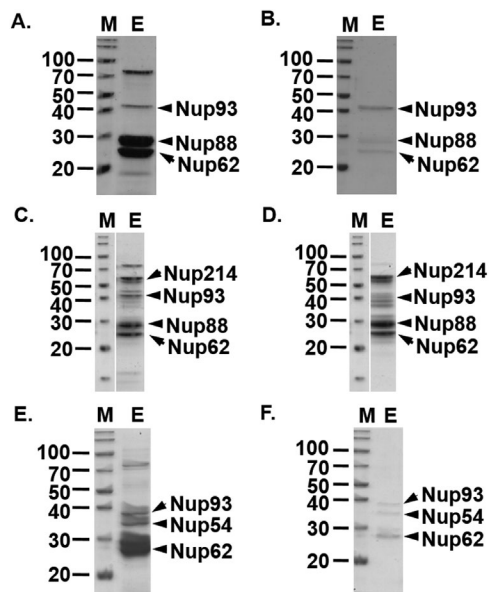
FIGURE 9: Interaction analysis of N-terminal domain of Nup93 with Nup88•Nup62Nup88•Nup62•Nup214 and Nup62•Nup54 complexes: SDS–PAGE images showing the reconstituted complexes with Nup93$^{1-150}$ and their interaction via tandem affinity purification (Ni^{2+}-NTA affinity followed by GST affinity purification). (A, B) Nup88$^{517-742}$•Nup62$^{322-525}$ complex. (C, D) Nup88$^{517-742}$•Nup62$^{322-525}$•Nup214$^{693-976}$ complex. (E, F) Nup62$^{322-525}$•Nup54$^{181-507}$ complex. A, C, and E show the Ni^{2+}-NTA affinity elutions, while B, D, and F show GST-affinity elutions. M-marker, E-eluted fractions.

recent study, which used the hNup93 construct boundary as 2–93 to interact with Nup88$^{559-741}$•Nup62$^{317-522}$•Nup214$^{699-888}$ (Bley *et al.*, 2022). Additionally, we observed the existence of a stable complex of Nup93$^{1-150}$ with the Nup88$^{517-742}$•Nup62$^{322-525}$ heterotrimer.

Mammalian Nup62•Nup54 heterotrimer can also bind with the N-terminal region of Nup93

Previously it was reported that Nup62 along with Nup54 can form a stable heterotrimer (Solmaz *et al.*, 2011) and its minimal coiled-coil domain structure was revealed using x-ray crystallography showing two helices of Nup62 interacting with one helix of Nup54. Interestingly, in this case also, it is observed that the mammalian Nup62•Nup54•Nup58 heterotrimer is highly dynamic and Nup58 can be easily dissociated to form the Nup62•Nup54 complex (Sharma *et al.*, 2015). We found such observation remarkably similar to our reported data in the case of Nup88$^{517-742}$•Nup62$^{322-525}$ and Nup88$^{517-742}$•Nup62$^{322-525}$•Nup214$^{693-976}$ complexes. Therefore, we made an assumption that, similar to the Nup88$^{517-742}$•Nup62$^{322-525}$ heterotrimer, the Nup62$^{322-525}$•Nup54$^{181-507}$ heterotrimer may bind to the Nup93$^{1-150}$ region. To prove this, we coexpressed proteins human Nup54 (181–507 region; all structured), Nup93$^{1-150}$, and Nup62$^{322-525}$ and performed TAP experiments as described above. The SDS–PAGE analysis clearly indicated that the mammalian Nup62•Nup54 heterotrimer is capable of interacting with Nup93$^{1-150}$ in a stable manner as it has not dissociated in our TAP experiments (Figure 9, E and F). The presence of the three proteins was also confirmed in Western blotting analysis using anti-His$_6$, anti-GST, and anti-Nup54 antibodies (Supplemental Figure S14). This led us to conclude that the Nup93$^{1-150}$ region is capable of binding with compositionally different yet structurally similar heterotrimers such as Nup88$^{517-742}$•Nup62$^{322-525}$, Nup88$^{517-742}$•Nup62$^{322-525}$• Nup214$^{693-976}$, Nup62$^{322-525}$•Nup54$^{181-507}$

(described in this study), and Nup62•Nup54•Nup58 (described in Sonawane *et al.*, 2020). Such a phenomenon of multipartner protein interface clusters that can adaptively bind to different proteins due to their conserved binding pocket is also known in other cases in the literature (Keskin and Nussinov, 2007).

DISCUSSION

The CR of the mammalian NPC is an important platform for mRNA export and is linked to several diseases. To gain insights into interdomain interactions and structural aspects, we focused on the mammalian Nup88•Nup62•Nup214 complex, which is positioned in the CR along with the Y-shape complex. In this study, we demonstrate for the first time, the extensive interaction network and biochemical reconstitution of the mammalian Nup88$^{517-742}$•Nup62$^{322-525}$ and Nup88$^{517-742}$•Nup62$^{322-525}$•Nup214$^{693-926}$ complex. We observed that most of the interacting regions are conserved between the mammalian and corresponding complexes in fungal species (Gaik *et al.*, 2015; Teimer *et al.*, 2017), indicating that the coiled-coil domains of Nup62, Nup88, and Nup214 drive the conserved core assembly of the CR complex. Nup62 is also a key component to form the CTC complex as reported previously (Bailer *et al.*, 2000; Solmaz *et al.*, 2011) in similar stoichiometry and molecular arrangement; it is therefore reasonable to propose that the Nup62 coiled-coil domain, which is highly dynamic in nature (Dewangan *et al.*, 2017), plays an important role in providing the plasticity of both the CR and the CTC complex.

The biochemical reconstitution followed by extensive characterization using CD spectroscopy, SAXS, EM, and SEC-MALS analysis of Nup88$^{517-742}$•Nup62$^{322-525}$•Nup214$^{693-926}$ and Nup88$^{517-742}$•Nup62$^{322-525}$ heterotrimers established that they both could form heterotrimeric assemblies, which is highly dynamic in nature. Our studies also established that the Nup88$^{517-742}$•Nup62$^{322-525}$ complexes exhibit a highly elongated conformation, and incorporation of Nup214$^{693-926}$ into Nup88$^{517-742}$•Nup62$^{322-525}$ formed a slightly more stable heterotrimer that results in a compact conformation (Figure 8D). The low-resolution 3D structure revealed by negatively stained EM of the Nup88$^{517-742}$•Nup62$^{322-525}$•Nup214$^{693-926}$ complex showed an elongated density with a bulky and curved head. It displayed an unusual asymmetric "4"-shaped structure where helical regions of all three Nups can be modeled. It is noteworthy that the affinity purification of the Nup88$^{517-742}$•Nup62$^{322-525}$•Nup214$^{693-926}$ complex although appearing to have 1:1:1 stoichiometry, shows highly dynamic behavior, and it is likely that various stoichiometric combinations may coexist together in solution, including Nup88$^{517-742}$•Nup62$^{322-525}$ and Nup88$^{517-742}$•Nup62$^{322-525}$•Nup214$^{693-926}$ heterotrimers, as evident by the broad SEC eluted peak profile (Figure 5, D and E). Therefore it is plausible that both heterotrimeric populations might have existed on the uranyl acetate–stained EM grids (Figure 8A); however, we might have enriched the Nup88$^{517-742}$•Nup62$^{322-525}$•Nup214$^{693-926}$ heterotrimer population by particle selection as it is biased toward selecting more globular and compact structures. Additionally, our CD-based analysis has demonstrated that the Nup88$^{517-742}$•Nup62$^{322-525}$•Nup214$^{693-926}$ heterotrimer is more thermally stable and structured in comparison to the Nup88$^{517-742}$•Nup62$^{322-525}$ heterotrimer (Figure 7 and Supplemental Table S5).

Our interaction analysis demonstrated a direct physical interaction of the β-propeller domains of Nup88$^{59-498}$ and Nup214$^{1-407}$ (Figure 3B), and the Nup214$^{1-407}$•Nup88$^{59-498}$ complex is stable enough for biochemical purification (Supplemental Figure S7c). Also, this β-propeller domain complex is expected to occupy the bottom of the Nup88•Nup62•Nup214 complex (Figure 10A). The
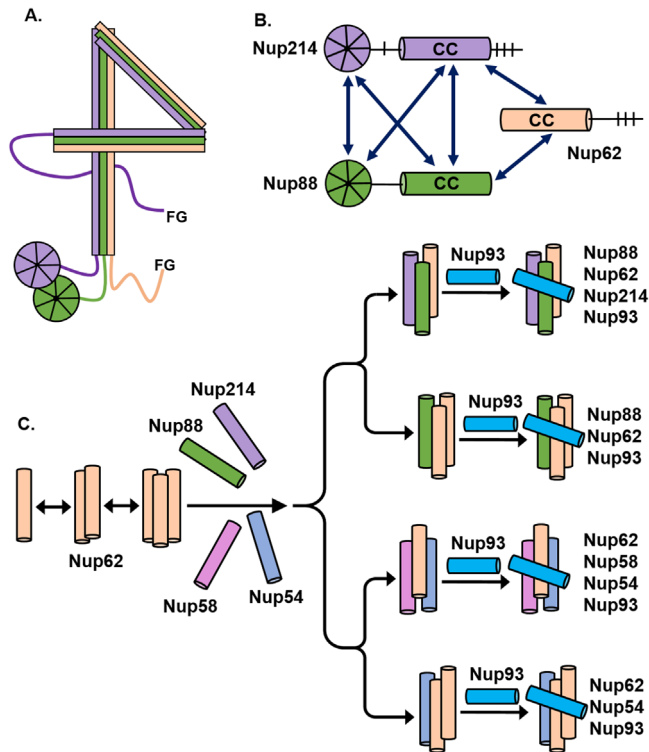
FIGURE 10: Role of Nup62 and Nup93 as hub proteins in the mammalian NPC. (A) Cartoon representation of "4" shape structure adopted by the coiled-coil domains of the Nup88•Nup62•Nup214 complex and showing β-propeller domain interaction of Nup88 and Nup214. (B) Summary of the interdomain interaction network among the three Nups. (C) Cartoon representation of coiled-coil domain of Nup62 (orange), Nup88 (green), Nup214 (purple), Nup54 (cyan), and Nup58 (pink). The plasticity exhibited by the Nup62 coiled-coil domain allows it to interact with other Nups and form various heterotrimers such as Nup88$^{517-742}$•Nup62$^{322-525}$, Nup88$^{517-742}$•Nup62$^{322-525}$•Nup214$^{693-976}$, Nup62$^{322-525}$•Nup54$^{181-507}$, and Nup62•Nup54•Nup58. Such heterotrimers are further recognized by the N-terminal (1–150) of Nup93 (blue) to form distinct quaternary complexes.

β-propeller domain of Nup214 is known to bind the mRNA export factor DDX19/Dbp5 (Schmitt *et al.*, 1999; Weirich *et al.*, 2004; von Moller *et al.*, 2009), while the β-propeller domain of Nup88 binds to the autoproteolytic domain (APD) of Nup98 (Stuwe *et al.*, 2012; Bley *et al.*, 2022). Our finding reveals that the β-propeller domains of Nup88$^{59-498}$ and Nup214$^{1-407}$ can also form a biochemically stable complex, thus showing an additional feature in the interaction network of the Nup88, Nup214, and Nup98 (APD) domain within the NPC. However, it is yet to be seen whether the Nup98 (APD domain) and β-propeller domains of Nup88 and Nup214 can form a heterotrimeric complex or interact in a mutually exclusive manner. These interactions may have a direct role in mRNA export and remodeling, and it is yet to be shown how the cross-talk between the β-propeller domains of Nup214 and Nup88 can influence mRNA export.

We have previously reported the low-resolution EM structure of the mammalian Nup62$^{322-525}$•Nup58$^{239-415}$•Nup54$^{332-510}$•Nup93$^{1-819}$ quaternary complex (Sonawane *et al.*, 2020), and we observed remarkable similarity with the Nup88$^{517-742}$•Nup62$^{322-525}$•Nup214$^{693-926}$ heterotrimeric EM map (Figure 8D). Hence, we conclude that both complexes adopt similar architectural arrangements of the coiled-coil domains. Notably, it has been reported that in *C. thermophilum*,

the Nsp1•Nup49•Nup57 complex (homologue of Nup62•Nup58•Nup54) is structurally related to the Nup82•Nup159•Nsp1 complex (situated in the CR), as both complexes assume similar triple helix coiled-coil "4"-shaped architectures (Chug *et al.*, 2015; Fernandez-Martinez *et al.*, 2016; Teimer *et al.*, 2017). Such structural similarity is further demonstrated in our data where we showed that Nup93$^{1-150}$ could bind to Nup88$^{517-742}$•Nup62$^{322-525}$•Nup214$^{693-976}$ heterotrimers (Figure 9) in a similar manner as reported previously for the Nup62•Nup54•Nup58 complex (Sonawane *et al.*, 2020). On the basis of all this evidence, we propose that Nup62 is a hub protein of the NPC to form distinct biochemically stable heterotrimers (Nup62$^{322-525}$•Nup88$^{517-742}$•Nup214$^{693-976}$, Nup88$^{517-742}$•Nup62$^{322-525}$, Nup62$^{322-525}$•Nup54$^{181-507}$, and Nup62•Nup54•Nup58 complexes), and this ability is exhibited due to dynamic behavior of its coiled-coil domain (Figure 10C).

The dynamic nature of the CTC complex is well documented for mammalian and yeast species (Ulrich *et al.*, 2014; Sharma *et al.*, 2015; Dewangan *et al.*, 2017), where the varying stoichiometry is interpreted based on biochemical reconstitution of the structured regions of Nup62 (Nsp1), Nup54 (Nup57), and Nup58 (Nup49). This variation in the CTC complex stoichiometry is mainly attributed to its intrinsic plasticity, and the biochemical purification strategies seem to enrich a selective combination, thus giving the false notion of 1:1:1 stoichiometry (Sonawane *et al.*, 2020). Moreover, the crystal structures of the structure regions of the CTC complexes from fungal (bound to the Nic96 N-terminal helix) and *Xenopus* species (without Nup93) (Chug *et al.*, 2015; Stuwe *et al.*, 2016a) also indicated 1:1:1 stoichiometry of the CTC complexes. It is to be noted that these complexes were stabilized using nanobodies and thus may not represent the true dynamic nature of the CTC complex (Chug *et al.*, 2015; Stuwe *et al.*, 2016a). All together it is now clear that the dynamic nature of the CTC complex is an evolutionarily conserved phenomenon and may play a role in the NPC-mediated nucleocytoplasmic transport. Notably, earlier it was thought that only the Nup62•Nup54•Nup58 heterotrimer could bind to Nup93. Our current biochemical study clearly demonstrates that Nup62 shared other heterotrimers (Nup62$^{322-525}$•Nup54$^{181-507}$ and Nup88$^{517-742}$•Nup62$^{322-525}$) are fully capable of binding to the Nup93$^{1-150}$ (Figure 9). The existence of such dynamic heterotrimers and their anchorage to Nup93 are yet to be demonstrated in vivo. Nonetheless, considering the versatile transport activity of the NPC, it is plausible that these heterotrimers might play a role in regulating transport function, which is primarily driven by the interaction of the FxFG/FG regions of these Nups with the transporting cargoes (Bayliss *et al.*, 2000).

Previously, biochemically reconstituted hydrogel studies have shown that the FG regions and FG-like regions of *Xenopus* Nup62, Nup54, and Nup58 together provide a complete passive diffusion barrier (Labokha *et al.*, 2013). However, the hydrogels derived from the FG and FG-like regions of Nup54 and Nup58 alone did not show such a passive diffusion barrier. Notably, the hydrogel constituted of FG regions of Nup62 alone showed a partial passive diffusion barrier (Labokha *et al.*, 2013). Hence we can imagine a scenario within a NPC where Nup62•Nup54•Nup58 heterotrimers anchored with Nup93 will provide a complete diffusion barrier; however, when one of the Nup62-interacting partners is missing, a heterotrimer such as Nup62•Nup54 would still be able to anchor to the Nup93, but its passive diffusion barrier would be altered. Such possibilities hence could guide us in understanding the mechanistic regulation of nucleocytoplasmic transport.

Based on a *Xenopus* cryo-ET study, the central channel is shown to undergo significant structural rearrangement when transcription

is blocked (Eibauer *et al.*, 2015), Recently, human NPC cryo-ET revealed substantial plasticity in its structure and it is believed that the structural plasticity might be due to compositional variation, which is driven by the cellular context (Schuller *et al.*, 2020). Additionally, it has been shown that Nup62, Nup58, and Nup54 undergo major conformational changes when transport through the NPC is altered (Pulupa *et al.*, 2020). On the basis of our data here and evidence from other studies (Labokha *et al.*, 2013; Eibauer *et al.*, 2015; Pulupa *et al.*, 2020; Schuller *et al.*, 2020), we propose that diverse Nup62 shared CTC heterotrimers could exist within a NPC and contribute to modulating the diffusion barrier. Moreover, as Nup62 is demonstrated to be a part of the exocyst complex and centrosome as well (Hubert *et al.*, 2009; Hashizume *et al.*, 2013; Dewangan *et al.*, 2017; Chien *et al.*, 2020), it is possible that the non–NPC related Nup62 shared heterotrimers might also have some functional specificity in these cellular functions that are yet to be explored. Similarly, recent cryo-ET–based studies of the *Xenopus* NPC also revealed substantial plasticity in the Nup88•Nup62•Nup214 complex organization with the NPC as clear density for one copy of the complex could be seen; however, the density for the second copy is partially visible (Fontana *et al.*, 2022). Notably, the electron density for the β-propeller domain of Nup214 is not clearly understood in this study (Fontana *et al.*, 2022). This indicates that similar to the CTC complexes, the Nup88 complexes are also highly dynamic and compositional variations might exist together.

Nup93 is also central to NPC organization; it can interact with Nup188, Nup35, Nup205, and Nup155 along with the CTC complexes (Fischer *et al.*, 2015). Recently, a *Xenopus* oocyte nuclei cryo-ET study revealed that Nup93 bridges the CR complex with the Y shape complex (Fontana *et al.*, 2022). It was also reported previously that the N-terminal region of human Nup93[1-150] has two short helices (1–82 and 96–150) that can preferentially interact with other partners, for example, region 1–82 interacts with the CTC complex in 1:1:1:1 stoichiometry (Sonawane *et al.*, 2020). In the case of both fungal and mammalian CTC, so far only the Nup62•Nup54•Nup58 complex is shown to interact with Nup93 (Stuwe *et al.*, 2016a; Sonawane *et al.*, 2020). Although it was reported earlier that rat and the corresponding yeast Nup62•Nup54 also form a complex (Solmaz *et al.*, 2011; Ulrich *et al.*, 2014) but its relevance with Nup93 interaction was not clear. Here, we show that the N-terminal region of Nup93[1-150] can bind to a diverse set of heterotrimers formed by Nup62, including the Nup62[322-525]•Nup54[181-507] and Nup88[517-742]•Nup62[322-525] heterotrimers. It is therefore plausible that Nup62 shares various heterotrimers that pose a specific binding pocket that can be recognized by Nup93. Such shared organizational behavior of Nups is very intriguing in terms of NPC assembly and its versatile transport function.

In the case of multipartner protein, a hub protein is defined as a protein with the conserved domain/motif that can interact with multiple partners (Ekman *et al.*, 2006) and show highly clustered functional modules. In the case of Nup93 and Nup62, it is shown that both are essential for cell viability and proper NPC organization (Grandi *et al.*, 1993; Allende *et al.*, 1996; Galy *et al.*, 2003; Osmani *et al.*, 2006; Sachdev *et al.*, 2012; Kinoshita *et al.*, 2014). The role of Nup93 in NPC assembly and the role of Nup62 in mRNA export and mitosis have been extensively studied (Galy *et al.*, 2003; Sachdev *et al.*, 2012; Hashizume *et al.*, 2013; Fernandez-Martinez *et al.*, 2016; Okazaki *et al.*, 2020). Moreover, their functions are evolutionarily conserved. Our study here suggests that Nup93 and Nup62 meet these criteria to be hub proteins and thus enable us to undertake further studies to refine their role in transport activity in a Nup-specific manner.

Interestingly, it has been shown that the overall structures of the Nup88 complex and its homologue in yeast (Nup82 complex) are similar (Gaik *et al.*, 2015; Fernandez-Martinez *et al.*, 2016) but their interactions with other Nups could be different. For instance, the mammalian Nup88 complex interacts with the N-terminal of Nup93 as described here. However, in fungi, the corresponding homologue Nup82 complex does not bind to the N-terminal of Nic96 (homologue of Nup93); rather it interacts with Nup145C (Teimer *et al.*, 2017; Bley *et al.*, 2022). This highlights the fact that although both CTC and the Nup88/82 complexes are conserved between unicellular and vertebrate NPC, their anchorage to the NPC framework might be mediated by two different partners, namely Nup145C and Nup93, respectively. It will be interesting to understand further how these differences would lead to species-specific arrangement of the IR and CR.

The human CR Nups and their associated mRNA export factors are recognized as important players in multiple disease conditions (Köhler and Hurt, 2010; Yarbrough *et al.*, 2014; Ciomperlik *et al.*, 2015; Nofrini *et al.*, 2016; Lin and Hoelz, 2019) and are suggested to govern the remodeling of mRNPs at the cytoplasmic face of the NPC (Belgareh *et al.*, 1998; Bailer *et al.*, 2000; Hutten and Kehlenbach, 2006; Napetschnig *et al.*, 2007; Kalverda *et al.*, 2010). Therefore, ultimate mechanistic insights of these Nups will be feasible by high-resolution structural analysis, which could not be pursued for mammalian Nup88 complexes until now, mainly due to the lack of biochemical reconstitution. Our interaction and reconstitution data here suggested a hub role for Nup62 in assembling both the Nup88 complex (constituent of CR) and CTC complexes and the role of Nup93 in their anchorage to the NPC framework, thus laying the groundwork for atomic resolution structural studies in the future.

MATERIALS AND METHODS
Sequence analysis of Nups
A total of 38 sequences were obtained from Uniprot (Supplemental Table S1) for each Nup and were aligned by MUltiple Sequence Comparison by Log Expectation (MUSCLE). The sequences were assembled to a neighbor-joining tree using MEGA 6 (Tamura *et al.*, 2013), and the bootstrap was calculated with 1000 replications. The final trees were edited and viewed using the iTOL tool (Letunic and Bork, 2019). The sequence alignment (structure guided) of rats, humans, *Xenopus*, *Danio*, *Chaetomium*, and *Saccharomyces* was done using PROMALS3D (Pei *et al.*, 2008) and edited in Jalview (Waterhouse *et al.*, 2009) to remove the low-complexity FG repeat regions and Jpred (Drozdetskiy *et al.*, 2015) to predict the secondary structures considering *Rattus norvegicus* Nup as a template. The domain organizations based on the secondary structure predictions for Nups were performed using the PSIPRED server (Jones, 1999), and the sequences were visualized using the IBS illustrator (Liu *et al.*, 2015).

CoRNeA
CoRNeA was performed using primary amino acid sequences from both proteins in a complex as the input information as described in Chopra *et al.* (2020). Only the structured regions of Nup88[1-742], Nup62[320-525], and Nup214[1-1100] were considered for the predictions.

Generation of *Escherichia coli*-based overexpression plasmids
The total RNA was isolated from rat spleen using the Trizol reagent (Invitrogen), and cDNA was prepared with the Superscript-II synthesis kit (Invitrogen) following the manufacturer's instructions. The

gene-specific primers (Supplemental Table S6) for Nup88[517-742], Nup62[322-525], and Nup214[693-976] were used to amplify various deletion constructs using Phusion polymerase (NEB). The α-helix of Nup62[322-525] and the α-helix as well as β-propeller regions of Nup88[59-498] and Nup214[1-407] were cloned into the respective vectors (refer to Supplemental Table S6). In all cases, affinity tags were removed by thrombin digestion. All positive clones were confirmed by gene sequencing.

In vitro pull-down assay

pET28a and pGEX4T1 vectors having respective genes (Supplemental Table S6) were cotransformed into *E. coli* BL21 (DE3) RIL cells. Rat His$_6$-Nup62[322-525] was subcloned into the pET28a vector using a construct described in Melcak *et al.* (2007), which was gifted by the Blobel lab. For the negative control for pull-down experiments, the empty pGEX4T1 vector cotransformed with pET28a expressing Nup88 (β-propeller; 59–498) and pET28 expressing Nup88 (α-helix; 322–525; β-propeller; 59–498) and pGEX4T1 expressing Nup62 (α-helix; 322–525) and Nup214 (β-propeller; 1–407) were transformed separately. All the experiments were repeated at least three times. Briefly, the bacterial culture was grown at 37°C until the OD$_{600}$ reached 0.6, induced with 0.4 mM of Isopropyl β-D-1-thiogalactopyranoside [IPTG] (MP Biomedicals) and incubated for 14–16 h at 18°C. The bacterial cells were harvested and lysed in lysis buffer (20 mM Tris-HCl, pH 8, 250 mM NaCl, 1 mM phenylmethylsulfonyl fluoride (PMSF), 5 mM beta mercaptoethanol (β-Me), 10 mM imidazole, 10% glycerol, and 1% Triton X-100). The clear lysate was incubated with Ni^{2+}-NTA agarose beads (Qiagen) for 2 h at 4°C. The unbound fractions were discarded, and the beads were washed with 40 column volumes (CV) of wash buffer (20 mM Tris-HCl, pH 8, 250 mM NaCl, 5 mM β-Me, 35 mM imidazole, 2.5% glycerol, and 0.1% Triton X-100). Bound fractions were eluted with elution buffer (20 mM Tris-HCl, pH 8, 250 mM NaCl, 5 mM β-Me, 300 mM imidazole, 2.5% glycerol, and 0.05% Triton X-100). Ni-NTA–eluted fractions were incubated with GSH-Sepharose (Pierce) beads for 5 h at 4°C. The unbound fractions were discarded, and the beads were washed with 40 CV of wash buffer (with 0.05% Triton X-100). Bound fractions were eluted with elution buffer (with 10 mM reduced glutathione). The eluted fractions from each pull down (Ni^{2+}-NTA and GST-affinity) were probed with anti-GST (1:3000) antibody (Sigma) and anti-His (1:3000) antibody (Sigma). Horseradish peroxidase–conjugated mouse immunoglobulin G was used at 1:5000 dilution (Sigma) for developing the signal and all the images were captured using Amersham Imager 600 and 800 (GE Healthcare).

Protein purification

To purify the Nup88•Nup62•Nup214 complex, a pRSFDuet1 vector expressing Nup88[517-742] and Nup62[322-525] was cotransformed with pGEX4T1 expressing Nup214[693-976] into the BL21 (RIL) cells. The protein was overexpressed as described above and lysed using the lysis buffer mentioned previously followed by centrifugation. The clear lysate was incubated with Ni^{2+}-NTA (Qiagen) beads for 2–3 h at 4°C and washed with a 40× CV of wash buffer followed by elution. For the second affinity step, the Ni^{2+}-NTA–eluted fractions were pooled, dialyzed, and incubated with GSH-Sepharose (Pierce) beads. The bound complexes were eluted with a wash buffer having 10 mM reduced glutathione (Sigma). Eluted fractions were then concentrated with a 10 kDa concentrator (Amicon Ultra; Merck), and both His$_6$ and GST tags were cleaved with 5–10 U of thrombin (Merck) per milligram of protein for 24 h at 4°C and subjected to SEC using the Superdex 200 10/30 GL column, preequilibrated with

SEC buffer (20 mM Tris-HCl, pH 8, 150 mM NaCl, 0.5 mM EDTA, and 1 mM dithiothreitol [DTT]). The entire purification was analyzed using SDS–PAGE. To purify the Nup88•Nup62 binary complex, the pRSFDuet-1 expressing Nup88[517-742] and Nup62[322-525] was similarly overexpressed and purified as mentioned above. For the purification of Nup88[517-742] and Nup62[322-525], pET28a constructs were used and proteins were purified using Ni^{2+}-NTA affinity chromatography. The buffer composition for Nup62 was similar except for the detergent and glycerol, while for Nup88, 0.05% detergent was used. To purify the Nup88•Nup62•Nup214•Nup93 complex, the bacterial cells having Nup88•Nup62•Nup214 and Nup93[1-150] were expressed separately and colysed, purified by tandem affinity pull down. For the Nup88•Nup62•Nup93 complex, Nup88•Nup62 and Nup93[1-150] were coexpressed and purified by tandem affinity pull down. The buffer compositions were the same as those mentioned above. The constructs for Nup54[181-507]•Nup93[1-150] and Nup62[322-525] were cotransformed, overexpressed, and purified using Ni^{2+}-NTA followed by GST pull down as described earlier (Sonawane *et al.*, 2020).

Mass spectrometry–based confirmation of the Nup88•Nup62•Nup214 complex

The SEC-eluted fraction and SDS–PAGE bands corresponding to the complex were subjected to trypsin digestion and investigated using the Orbitrap analyzer, and the obtained data were analyzed using Proteome Discoverer 2.2 (Thermo Fisher) software.

SEC-MALS

The purified individual Nups and complexes at various concentrations (Supplemental Table S4) were analyzed with SEC using either Superdex 200 10/30 GL or Superose6 increase 10/30 GL column coupled with a MALS instrument (Wyatt Technology). The chromatography system was connected in series with a light-scattering detector (Wyatt Dawn HELIOS II) and refractive index detector (Wyatt Optilab t-rEX). Bovine serum albumin (2 mg/ml) (Sigma) was used as a standard to calibrate the system, and 100 µl of each sample was injected. The column was equilibrated with the SEC buffer. Data analysis was carried out using the program ASTRA (Wyatt Technology), yielding the molar mass and mass distribution (polydispersity) of the samples.

CD analysis and thermal denaturation

CD spectra of SEC-purified proteins (0.15–0.2 mg/ml) were recorded using a Jasco J-815 (Jasco, Tokyo, Japan) spectropolarimeter at 25°C. The proteins in 10 mM Tris-Cl (pH 8.0), 50 mM NaCl, and 1 mM DTT used for far-UV CD spectra were recorded in a rectangular quartz cuvette of 1 mm path length in the range of 200–250 nm at a scan speed of 100 nm/min with slit width of 1 nm. Each spectrum was recorded as an average of three accumulations and was corrected for buffer contributions before analysis. The observed values were converted to mean residue ellipticity (MRE) using the equation MRE = $M\theta/10dcr$, where M is the molecular weight of the protein, θ is the CD in millidegrees, d is the path length in centimeters, c is the protein concentration in milligrams per milliliter, and r is the average number of amino acid residues in the protein. The relative content of secondary structure elements was calculated using CDPro software and the CONTINLL program, which gave the smallest NRMSD (normalized root mean square deviation) value. The percent helicity (α-helix content) was calculated from the MRE value at 222 nm, using the equation % α-helix = (MRE$_{222nm}$/MRE$_{max}$) × 100, where MRE$_{max}$ = –23400 (Wang *et al.*, 2006). For thermal denaturation studies, the protein sample was incubated at varying temperatures from 25 to

85°C with an interval of 5°C for 5 min each. The melting temperatures of the proteins/complexes were calculated by scattering the ellipticity at 208 and 222 nm, followed by sigmoidal fit analysis.

SAXS analysis

Purified Nup88$^{517-742}$•Nup62$^{322-525}$ complex (0.9 mg/ml) was used to collect scattering data at the European Synchrotron Radiation Facility (ESRF), Grenoble, France, on beamline BM29 (λ = 0.991 Å) in a standard setup (Pernot et al., 2013). A total of 10 frames were collected (0.5 s/frame) at 277 K on a PILATUS 1M detector and the sample-to-detector distance was 2.87 mm. Sample buffer (SEC buffer) was used as control for buffer scattering data set subtraction automatically via EDNA (Incardona et al., 2009). Scattering data sets collected were analyzed using ATSAS 2.8 (Franke et al., 2017). The initial molecular envelope was built using DAMMIF. CRYSOL was used to obtain the theoretical I (Q) profile of the model and to compare it with the I (Q) profile of raw data.

Negative staining and EM

Purified protein complex (4 µl) (Nup88$^{517-742}$•Nup62$^{322-525}$•Nup214$^{693-926}$; 0.05 mg/ml) was adsorbed onto a glow-discharged, carbon-coated 300 mesh copper grid for 2 min, and the excess sample was blotted away using Whatman filter paper. Then, 4 µl of 2% uranyl acetate adjusted to pH 7.4 was applied on the grid twice for 2 min each time. The grids were again blotted to remove excess stain and air dried overnight. The grids were loaded on JEM 220FS (Jeol) accelerated at 200 kV with a field emission gun. Fifty-four micrographs were collected and subjected to single particle analysis using CryoSPARC (Punjani et al., 2017) using MotionCorr2, and CTF estimation was performed using CTFFIND4 implemented in RELION 3.1.0 (Zivanov et al., 2018). After several rounds of 2D classification followed by manual inspection, a total 4737 particles were selected for ab initio reconstruction. Homogeneous refinement was performed using a 3D map to obtain the final resolution. The homology model of the complex was built using CTC•Nic96^{R1} complex (Stuwe et al., 2016a; PDB; 5CWS) structure as a template in SWIS MODEL (Schwede et al., 2003). Additional regions were modeled using the Alpha fold model of Nup88 and Nup214 and fitted into the EM density map as the rigid body using UCSF chimera (Pettersen et al., 2004).

REFERENCES

Alber F, Dokudovskaya S, Veenhoff LM, Zhang W, Kipper J, Devos D, Suprapto A, Karni-Schmidt O, Williams R, Chait BT, et al. (2007). The molecular architecture of the nuclear pore complex. Nature 450, 695–701.

Allende ML, Amsterdam A, Becker T, Kawakami K, Gaiano N, Hopkins N (1996). Insertional mutagenesis in zebrafish identifies two novel genes, pescadillo and dead eye, essential for embryonic development. Genes Dev 10, 3141–3155.

Bailer SM, Balduf C, Katahira J, Podtelejnikov A, Rollenhagen C, Mann M, Pante N, Hurt E (2000). Nup116p associates with the Nup82p-Nsp1p-Nup159p nucleoporin complex. J Biol Chem 275, 23540–23548.

Bayliss R, Littlewood T, Stewart M (2000). Structural basis for the interaction between FxFG nucleoporin repeats and importin-beta in nuclear trafficking. Cell 102, 99–108.

Beck M, Hurt E (2017). The nuclear pore complex: understanding its function through structural insight. Nat Rev Mol Cell Biol 18, 73–89.

Belgareh N, Snay-Hodge C, Pasteau F, Dagher S, Cole CN, Doye V (1998). Functional characterization of a Nup159p-containing nuclear pore complex. Mol Biol Cell 9, 3475–3492.

Bley CJ, Nie S, Mobbs GW, Petrovic S, Gres AT, Liu X, Mukherjee S, Harvey S, Huber FM, Lin DH, et al. (2022). Architecture of the cytoplasmic face of the nuclear pore. Science 376, eabm9129.

Bui KH, von Appen A, DiGuilio AL, Ori A, Sparks L, Mackmull MT, Bock T, Hagen W, Andrés-Pons A, Glavy JS, Beck M (2013). Integrated structural analysis of the human nuclear pore complex scaffold. Cell 155, 1233–1243.

Burkhard P, Stetefeld J, Strelkov SV (2001). Coiled-coils: a highly versatile protein folding motif. Trends Cell Biol 11, 82–88.

Chien ML, Lai JH, Lin TF, Yang WS, Juang YL (2020). NUP62 is required for the maintenance of the spindle assembly checkpoint and chromosomal stability. Int J Biochem Cell Biol 128, 105843.

Chopra K, Bawaria S, Chauhan R (2019). Evolutionary divergence of the nuclear pore complex from fungi to metazoans. Protein Sci 28, 571–586.

Chopra K, Burdak B, Sharma K, Kembhavi A, Mande SC, Chauhan R (2020). CoRNeA: a pipeline to decrypt the inter-protein interfaces from amino acid sequence information. Biomolecules 10, 938.

Chug H, Trakhanov S, Hülsmann BB, Pleiner T, Görlich D (2015). Crystal structure of the metazoan Nup62•Nup58•Nup54 nucleoporin complex. Science 350, 106–110.

Ciomperlik JJ, Basta HA, Palmenberg AC (2015). Cardiovirus three leader proteins equivalently inhibit different nucleocytoplasmic and trafficking pathways. Virology 484, 194–202.

Cronshaw JM, Krutchinsky AN, Zhang W, Chait BT, Matunis MJ (2002). Proteomic analysis of the mammalian nuclear pore complex. J Cell Biol 158, 915–927.

Dewangan PS, Sonawane PJ, Chouksey AR, Chauhan R (2017). The Nup62 coiled-coil motif provides plasticity for triple-helix bundle formation. Biochemistry 56, 2803–2811.

Drozdetskiy A, Cole C, Procter J, Barton GJ (2015). JPred4: a protein secondary structure prediction server. Nucleic Acids Res 43(W1):W389–W394.

Eibauer M, Pellanda M, Turgay Y, Dubrovsky A, Wild A, Medalia O (2015). Structure and gating of the nuclear pore complex. Nat Commun 6, 7532.

Ekman D, Light S, Björklund AK, Elofsson A (2006). What properties characterize the hub proteins of the protein-protein interaction network of Saccharomyces cerevisiae? Genome Biol 7, R45.

Fernandez-Martinez J, Kim SJ, Shi Y, Upla P, Pellarin R, Gagnon M, Chemmama IE, Wang J, Nudelman I, Zhang W, et al. (2016). Structure and function of the nuclear pore complex cytoplasmic mRNA export platform. Cell 167, 1215–1228.e25.

Field MC, Rout MP (2019). Pore timing: the evolutionary origins of the nucleus and nuclear pore complex. F1000 Res 8, F1000 Faculty Rev-369.

Fischer J, Teimer R, Amlacher S, Kunze R, Hurt E (2015). Linker Nups connect the nuclear pore complex inner ring with the outer ring and transport channel. Nat Struct Mol Biol 22, 774–781.

Fontana P, Dong Y, Pi X, Tong AB, Hecksel CW, Wang L, Fu TM, Bustamante C, Wu H (2022). Structure of cytoplasmic ring of nuclear pore complex by integrative cryo-EM and AlphaFold. Science 376, eabm9326.

Franke D, Petoukhov MV, Konarev PV, Panjkovich A, Tuukkanen A, Mertens HDT, Kikhney AG, Hajizadeh NR, Franklin JM, Jeffries CM, Svergun DI (2017). Computer Programs ATSAS 2.8: comprehensive data analysis suite for small-angle scattering from macromolecular solutions. J Appl Crystallogr 50(Pt 4), 1212–1225.

Fujiwara Y, Kurokawa T, Takeshita K, Kobayashi M, Okochi Y, Nakagawa A, Okamura Y (2012). The cytoplasmic coiled-coil mediates cooperative gating temperature sensitivity in the voltage-gated H+ channel Hv1. Nat Commun 3, 816.

Gaik M, Flemming D, von Appen A, Kastritis P, Mücke N, Fischer J, Stelter P, Ori A, Bui KH, Baßler J, et al. (2015). Structural basis for assembly and function of the Nup82 complex in the nuclear pore scaffold. J Cell Biol 208, 283–297.

Galy V, Mattaj IW, Askjaer P (2003). Caenorhabditis elegans nucleoporins Nup93 and Nup205 determine the limit of nuclear pore complex size exclusion in vivo. Mol Biol Cell 14, 5104–5115.

Grandi P, Doye V, Hurt EC (1993). Purification of NSP1 reveals complex formation with "GLFG" nucleoporins and a novel nuclear pore protein NIC96. EMBO J 12, 3061–3071.

Greenfield NJ, Hitchcock-DeGregori SE (1993). Conformational intermediates in the folding of a coiled-coil model peptide of the N-terminus of tropomyosin and alpha alpha-tropomyosin. Protein Sci 1, 1263–1273.

Grossman E, Medalia O, Zwerger M (2012). Functional architecture of the nuclear pore complex. Annu Rev Biophys 41, 557–584.

Hashizume C, Moyori A, Kobayashi A, Yamakoshi N, Endo A, Wong RW (2013). Nucleoporin Nup62 maintains centrosome homeostasis. Cell Cycle 12, 3804–3816.

Hoelz A, Debler EW, Blobel G (2011). The structure of the nuclear pore complex. Annu Rev Biochem 80, 613–643

Huang G, Zhang Y, Zhu X, Zeng C, Wang Q, Zhou Q, Tao O, Liu M, Lei J, Yan C, Shi Y (2020). Structure of the cytoplasmic ring of the *Xenopus laevis* nuclear pore complex by cryo-electron microscopy single particle analysis. Cell Res 30, 520–531.

Hubert T, Vandekerckhove J, Gettemans J (2009). Exo70-mediated recruitment of nucleoporin Nup62 at the leading edge of migrating cells is required for cell migration. Traffic 10, 1257–1271.

Hurt E, Beck M (2015). Towards understanding nuclear pore complex architecture and dynamics in the age of integrative structural analysis. Curr Opin Cell Biol 34, 31–38.

Hutten S, Kehlenbach RH (2006). Nup214 is required for CRM1-dependent nuclear protein export *in vivo*. Mol Cell Biol 26, 6772–6785.

Incardona MF, Bourenkov GP, Levik K, Pieritz RA, Popov AN, Svensson O (2009). EDNA : a framework for plugin-based applications applied to X-Ray experiment online data analysis. J Synchrotron Radiat 16, 872–879.

Jones DT (1999). Protein secondary structure prediction based on position-specific scoring matrices. J Mol Biol 292, 195–202.

Kalverda B, Pickersgill H, Shloma VV, Fornerod M (2010). Nucleoporins directly stimulate expression of developmental and cell-cycle genes inside the nucleoplasm. Cell 140, 360–371.

Keskin O, Nussinov R (2007). Similar binding sites and different partners: implications to shared proteins in cellular pathways. Structure 341–354.

Kim SJ, Fernandez-Martinez J, Nudelman I, Shi Y, Zhang W, Raveh B, Herricks T, Slaughter BD, Hogan JA, Upla P, *et al.* (2018). Integrative structure and functional anatomy of a nuclear pore complex. Nature 555, 475–482.

Kinoshita Y, Hunter RG, Gray JD, Mesias R, McEwen BS, Benson DL, Kohtz DS (2014). Role for NUP62 depletion and PYK2 redistribution in dendritic retraction resulting from chronic stress. Proc Natl Acad Sci USA 111, 16130–16135.

Köhler A, Hurt E (2010). Gene regulation by nucleoporins and links to cancer. Mol Cell 38, 6–15.

Kosinski J, Mosalaganti S, von Appen A, Teimer R, DiGuilio AL, Wan W, Bui KH, Hagen WJ, Briggs JA, Glavy JS, *et al.* (2016). Molecular architecture of the inner ring scaffold of the human nuclear pore complex. Science 352, 363–265.

Labokha AA, Gradmann S, Frey S, Hülsmann BB, Urlaub H, Baldus M, Görlich D (2013). Systematic analysis of barrier-forming FG hydrogels from Xenopus nuclear pore complexes. EMBO J 32, 204–218.

Letunic I, Bork P (2019). Interactive Tree Of Life (iTOL) v4: recent updates and new developments. Nucleic Acids Res 47(W1), W256–W259.

Lin DH, Hoelz A (2019). The structure of the nuclear pore complex (an update). Annu Rev Biochem 88, 725–783.

Liu W, Xie Y, Ma J, Luo X, Nie P, Zuo Z, Lahrmann U, Zhao Q, Zheng Y, Zhao Y, *et al.* (2015). Sequence analysis IBS: an illustrator for the presentation and visualization of biological sequences. Bioinformatics 31, 3359–3361.

López-García P, Goktas M, Bergues-Pupo AE, Koksch B, Varón Silva D, Blank KG (2019). Structural determinants of coiled-coil mechanics. Phys Chem Chem Phys 21, 9145–9149.

Melcák I, Hoelz A, Blobel G (2007). Structure of Nup58/45 suggests flexible nuclear pore diameter by intermolecular sliding. Science 315, 1729–1732.

Mosalaganti S, Kosinski J, Albert S, Schaffer M, Strenkert D, Salomé PA, Merchant SS, Plitzko JM, Baumeister W, Engel BD, Beck M (2018). *In situ* architecture of the algal nuclear pore complex. Nat Commun 9, 2361.

Napetschnig J, Blobel G, Hoelz A (2007). Crystal structure of the N-terminal domain of the human protooncogene Nup214/CAN. Proc Natl Acad Sci USA 104, 1783–1788.

Nofrini V, Di Giacomo D, Mecucci C (2016). Nucleoporin genes in human diseases. Eur J Hum Genet 24, 1388–1395.

Okazaki R, Yamazoe K, Inoue YH (2020). Nuclear export of cyclin B mediated by the Nup62 complex is required for meiotic initiation in *Drosophila* males. Cells 9, 270.

Osmani AH, Davies J, Liu HL, Nile A, Osmani SA (2006). Systematic deletion and mitotic localization of the nuclear pore complex proteins of Aspergillus nidulans. Mol Biol Cell 17, 4946–4961.

Pei J, Kim BH, Grishin NV (2008). PROMALS3D: a tool for multiple protein sequence and structure alignments. Nucleic Acids Res 36, 2295–2300.

Pernot P, Round A, Barrett R, De Maria Antolinos A, Gobbo A, Gordon E, Huet J, Kieffer J, Lentini M, Mattenet M, *et al.* (2013). Upgraded ESRF BM29 beamline for SAXS on macromolecules in solution. J Synchrotron Radiat 20(Pt 4), 660–664.

Pettersen EF, Goddard TD, Huang CC, Couch GS, Greenblatt DM, Meng EC, Ferrin TE (2004). UCSF Chimera—a visualization system for exploratory research and analysis. J Comput Chem 25, 1605–1612.

Pulupa J, Prior H, Johnson DS, Simon SM (2020). Conformation of the nuclear pore in living cells is modulated by transport state. eLife 9, e60654.

Punjani A, Rubinstein JL, Fleet DJ, Brubaker MA (2017). CryoSPARC: algorithms for rapid unsupervised Cryo-EM structure determination. Nat Methods 14, 290–296.

Rout MP, Aitchison JD, Suprapto A, Hjertaas K, Zhao Y, Chait BT (2000). The yeast nuclear pore complex: composition, architecture, and transport mechanism. J Cell Biol 148, 635–651.

Sachdev R, Sieverding C, Flötenmeyer M, Antonin W (2012). C-terminal domain of Nup93 is essential for assembly of the structural backbone of nuclear pore complexes. Mol Biol Cell 23, 740–749.

Schmitt C, von Kobbe C, Bachi A, Panté N, Rodrigues JP, Boscheron C, Rigaut G, Wilm M, Séraphin B, Carmo-Fonseca M, Izaurralde E (1999). Dbp5, a DEAD-box protein required for mRNA export, is recruited to the cytoplasmic fibrils of nuclear pore complex via a conserved interaction with CAN/Nup159p. EMBO J 18, 4332–4347.

Schuller AP, Wojtynek M, Mankus D, Tatli M, Kronenberg-Tenga R, Regmi SG, Dip PV, Lytton-Jean AKR, Brignole EJ, Dasso M, *et al.* (2021). The cellular environment shapes the nuclear pore complex architecture. Nature 598, 667–671.

Schwartz TU (2017). The structure inventory of the nuclear pore complex. J Mol Biol 428(Pt A), 1986–2000.

Schwede T, Kopp J, Guex N, Peitsch MC (2003). SWISS-MODEL: an automated protein homology-modeling server. Nucleic Acids Res 31, 3381–3385.

Sharma A, Solmaz SR, Blobel G, Melčák I (2015). Ordered regions of channel nucleoporins Nup62, Nup54, and Nup58 form dynamic complexes in solution. J Biol Chem 290, 18370–18378.

Solmaz SR, Chauhan R, Blobel G, Melčák I (2011). Molecular architecture of the transport channel of the nuclear pore complex. Cell 147, 590–602.

Sonawane PJ, Dewangan SP, Madheshiya PK, Chopra K, Kumar M, Niranjan S, Ansari MY, Singh J, Bawaria S, Banerjee M, Chauhan R (2020). Molecular and structural analysis of central transport channel in complex with Nup93 of nuclear pore complex. Protein Sci 29, 2510–2527.

Stuwe T, Bley CJ, Thierbach K, Petrovic S, Schilbach S, Mayo DJ, Perriches T, Rundlet EJ, Jeon YE, Collins LN, *et al.* (2016a). Architecture of the nuclear pore inner ring complex. Science 350, 56–64.

Stuwe T, Correia AR, Lin DH, Paduch M, Lu VT, Kossiakoff AA, Hoelz A (2016b). Architecture of the nuclear pore complex coat. Science 347,1148–1152.

Stuwe T, von Borzyskowski LS, Davenport AM, Hoelz A (2012). Molecular basis for the anchoring of proto-oncoprotein Nup98 to the cytoplasmic face of the nuclear pore complex. J Mol Biol 419, 330–346.

Tai L, Zhu Y, Ren H, Huang X, Zhang C, Sun F (2022). 8 Å structure of the cytoplasmic ring of the *Xenopus laevis* nuclear pore complex solved by Cryo-EM and AI. Protein Cell 13, 760–777.

Tamura K, Stecher G, Peterson D, Filipski A, Kumar S (2013). MEGA6: molecular evolutionary genetics analysis version 6.0. Mol Biol Evol 30, 2725–2729.

Teimer R, Kosinski J, von Appen A, Beck M, Hurt E (2017). A short linear motif in scaffold Nup145C connects Y-complex with pre-assembled outer ring Nup82 complex. Nat Commun 8, 1107.

Tsuruda PR, Julius D, Minor DL Jr (2011). Coiled coils direct assembly of a cold-activated TRP channel. Neuron 51, 201–212.

Ulrich A, Partridge JR, Schwartz TU (2014). The stoichiometry of the nucleoporin 62 subcomplex of the nuclear pore in solution. Mol Biol Cell 25, 1484–1492.

Varadi M, Anyango S, Deshpande M, Nair S, Natassia C, Yordanova G, Yuan D, Stroe O, Wood G, Laydon A, *et al.* (2022). AlphaFold protein structure database: massively expanding the structural coverage of protein-sequence space with high-accuracy models. Nucleic Acids Res 50(D1), D439–D444.

Von Appen A, Kosinski J, Sparks L, Ori A, DiGuilio AL, Vollmer B, Mackmull MT, Banterle N, Parca L, Kastritis P, *et al.* (2015). In situ structural analysis of the human nuclear pore complex. Nature 526, 140–143.

von Moeller H, Basquin C, Conti E (2009). The mRNA export protein DBP5 binds RNA and the cytoplasmic nucleoporin NUP214 in a mutually exclusive manner. Nat Struct Mol Biol 16, 247–254.

Wang D, Chen K, Kulp Iii JL, Arora PS (2006). Evaluation of biologically relevant short α-helices stabilized by a main-chain hydrogen-bond surrogate. J Am Chem Soc 128, 9248–9256.

Waterhouse AM, Procter JB, Martin DM, Clamp M, Barton GJ (2009). Jalview version 2—a multiple sequence alignment editor and analysis workbench. Bioinformatics 25, 1189–1191.

Weirich CS, Erzberger JP, Berger JM, Weis K (2004). The N-terminal domain of Nup159 forms a beta-propeller that functions in mRNA export by tethering the helicase Dbp5 to the nuclear pore. Mol Cell 16, 749–760.

Yarbrough ML, Mata MA, Sakthivel R, Fontoura BMA (2014). Viral subversion of nucleocytoplasmic trafficking. Traffic 15, 127–140.

Yoshida K, Seo HS, Debler EW, Blobel G, Hoelz A (2011). Structural and functional analysis of an essential nucleoporin heterotrimer on the cytoplasmic face of the nuclear pore complex. Proc Natl Acad Sci USA 108, 16571–16576.

Zivanov J, Nakane T, Forsberg BO, Kimanius D, Hagen WJ, Lindahl E, Scheres SH (2018). New tools for automated high-resolution cryo-EM structure determination in RELION-3. eLife 7, e42166.